May 2022

Dosimetric Simulation of a Talbot-Lau X-Ray Interferometry System for Medical Diagnostic Radiography

Charles A. Zimmerman
Louisiana State University and Agricultural and Mechanical College

DOSIMETRIC SIMULATION OF A TALBOT-LAU X-RAY INTERFEROMETRY SYSTEM FOR MEDICAL DIAGNOSTIC RADIOGRAPHY

A Thesis

Submitted to the Graduate Faculty of the
Louisiana State University and
Agricultural and Mechanical College
in partial fulfillment of the
requirements for the degree of
Master of Science

in

The Department of Physics and Astronomy

by
Charles Allan Zimmerman
B.S., University of Utah, 2019
August, 2022

Acknowledgments

This project was made possible by myriad individuals other than myself who deserve mentioning. I thank my advisor, Dr. Kenneth Matthews, for his wisdom, direction, and generosity. I also thank my supervisory committee co-chair, Dr. Wei-Hsung Wang, who acquired the funding for this project. I thank the other members of my supervisory committee, Dr. Les Butler, Dr. Joyoni Dey, and Dr. Matthew Penny for their time and insight. I thank Yao Zeng and Paige Whittington for their administrative jiu jitsu which more than once got me out of trouble.

I acknowledge the support of my many wonderful friends and colleagues among the LSU graduate student community. I thank James Taylor for providing the CT scan of the RANDO phantom and answering technical questions about the project. I thank Dan Neck for sleuthing out the material composition of the CT couch. I thank Dr. Fred Marazzato for his advice regarding engineering concepts and choice of FEA software.

Lastly, I thank Dr. Michelle Lis for her help organizing my thoughts, polishing my presentations, and proofreading my work. This project would surely have failed without her patient, thoughtful support.

Table of Contents

Nomenclature, Symbols, Acronyms

COPD	Chronic Obstructive Pulmonary Disease
CT	Computed Tomography
DICOM	Digital Imaging and Communications in Medicine
FEA	Finite Element Stress Analysis
GEANT4	Geometry And Tracking software
HU	Hounsfield unit
keV	kiloelectron volt
kVp	Peak kilovoltage
mA	milliamp
mGy	milligray
mSv	millisievert
nSv	nanosievert
NIST	National Institute of Standards and Technology
TLXI	Talbot-Lau X-ray Interferometry
TOPAS	TOol for PArticle Simulation

Abstract

Purpose: Lung cancer and other pulmonary disease is typically diagnosed by means of X-ray imaging, such as conventional radiography and computed tomography (CT). However, these modalities are not ideal for lung imaging due to their poor soft tissue contrast and the microscopic nature of early-stage disease. Diagnosis of lung disease could potentially be improved by an imaging modality which is as convenient and low-dose as current X-ray imaging, but provides better visualization of lung tissue.

Methods: We are developing chest radiography and CT systems for medical imaging which use a triple-grating Talbot-Lau X-ray interferometry (TLXI) design to extract dark-field and phase contrast information alongside a typical absorption image. The presence of the diffraction gratings and the requirements of the imaging protocol potentially impact patient radiation dose and image quality; assessing these impacts is key to maximizing image quality for minimum radiation dose. Furthermore, the effect on image quality of mechanical strain on the optical components has not been closely studied. We have produced software applications which employ 3D Monte Carlo particle transport techniques and finite element stress analysis (FEA) to calculate the radiation dose delivered to the patient for both radiography and CT and the rotation-induced deformation of the diffraction gratings for CT. A set of test cases were used to valid the software models. These numerical simulations will be used in the future to elucidate the relationship of image quality to acquisition parameters and grating design.

Results: The test cases confirmed that the geometry setup and output dosimetry data both meet real-world expectations. Our tests showed that the diagnostic X-ray beam interacts realistically with the diffraction gratings and patient volumes within the

simulation geometries. The FEA results also showed that rotational motion within the CT setup results in only small deformations to the structure of the optical components; the FEA results can be coupled to a model of TLXI signal propagation in the future to quantify any impact on image quality.

Conclusion: We have demonstrated the validity and functionality of our simulation models. The toolkit is ready for use in assessing prototype design to yield attenuation, dark-field, and phase contrast images of sufficient quality while remaining within acceptable dose tolerances. The addition of dark-field and phase contrast images to absorption images from radiography and CT is expected to enhance diagnosis of early-stage lung cancer and other pulmonary disease.

Chapter 1. Introduction

1.1. Goals

The diagnostic markers for lung malignancies tend to be difficult to detect in early stages. The early symptoms of chronic obstructive pulmonary disease (COPD), for instance, are subtle, heterogeneous, and ill-defined (Sidhaye *et al.*, 2018). COPD symptoms such as emphysema, airway wall thickening, and hyperinflation can be identified with chest radiography, but not with the sensitivity or specificity required for screening (Lynch, 2014). In the case of lung cancer, nodules as small as 2-5 millimeters in diameter are indicative of stage 1A disease (Henschke *et al.*, 1999). Malignant non-calcified nodules are often unremarkable in a conventional radiograph, but identifiable in a computed tomography (CT) image. Low-dose CT provides clinical information of comparable quality to standard CT and is currently the recommended modality for lung screening (Gierada *et al.*, 2007; Humphrey *et al.*, 2013). However, TLXI radiography systems have been shown to provide more potential information with less patient dose than low-dose CT (Yaroshenko *et al.*, 2015).

X-ray interferometry has the potential to enhance diagnosis of lung disease, by providing two additional types of images along with conventional absorption data. In particular, interferometry can visualize scattering properties of the lung-air interface which are strongly correlated to lung disease (Meinel *et al.*, 2014; Hellbach *et al.*, 2015). Triple-grating Talbot-Lau x-ray interferometry (TLXI) is one way to implement interferometry for lung radiography and CT. Dark field information from a TLXI system can enhance the sensitivity for both CT and radiography lung screening due to the

scattering properties of the lung-air interface (Scherer, Yaroshenko, *et al.*, 2017; Willer, Fingerle, Noichl, *et al.*, 2021).

Attenuation in the diffraction gratings and the multiple-image acquisition mode of TLXI potentially increases dose to the patient. Reducing the per-image dose so that total dose from a TLXI imaging procedure is acceptable is a key concern for developing viable clinical radiography and CT systems. Furthermore, grating stability may be impacted by mechanical strain imparted by CT gantry rotation. Developing modeling tools to study these concerns is the focus of this work. To that end, we have developed dose prediction and stress modeling applications for simulation of TLXI systems. The simulation models were validated by assessing the outputs of test geometries for consistency with physical expectations. The intention of this study was to demonstrate that our models produce results that have no statistically significant difference from expected physical behaviors, for instance exponential attenuation of a radiation beam.

1.2. Specific Aims

This project utilizes 3D Monte Carlo particle transport to calculate the radiation dose delivered to a patient and finite element stress analysis to determine grating design specifications. Our approach followed these specific aims:

1.2.1. Specific Aim 1

Simulate delivery of radiation under the radiography setup to determine acceptable acquisition parameters. We developed a GEometry ANd Tracking software (GEANT4; version 4-10-6 patch 3, Geant4 Collaboration, Meyrin, CH) application which transports a diagnostic x-ray beam through a voxelized phantom and TLXI diffraction gratings to the

detector plane. The application sets the X-ray spectrum according to acquisition parameters and emits a number of photons specified by the user. Stored event data is used to determine the photon count at the detector plane and the resulting radiation dose to the phantom.

1.2.2. Specific Aim 2

Simulate delivery of radiation under the computed tomography setup to determine acceptable acquisition parameters. The approach used in Specific Aim 1 was also implemented as a CT geometry. Volumes for the bow tie filter and imaging couch were incorporated into the model. The application models helical motion of scanner components based on pitch and time resolution parameters, emitting a user-specified number of photons at each gantry position. Stored event data is used to determine the photon count at the detector plane and the resulting radiation dose to the phantom.

1.2.3. Specific Aim 3

Simulate the motion of the computed tomography scanner to determine strain on the diffraction grating components. We designed a computational representation of grating-mount assemblies using Abaqus (SIMULIA ABAQUS FEA 2020 Student Edition; Dassault Systemes, Johnston, RI, USA). A static force equal to the centripetal force experienced during gantry rotation is applied to the surface of a grating according to the grating's distance from the center of rotation and the gantry's maximum angular velocity. The maximum displacement of the grating elements due to rotation-induced elastic deformation is calculated from Abaqus's output data.

1.3. Background

1.3.1. Diagnostic Imaging

Photon attenuation has been used in medical imaging since shortly after the discovery of X-rays in 1895. Attenuation imaging systems take advantage of the absorption and scattering interactions of photons with matter. This behavior is described as

$$N/N_0 = e^{-\mu' x}, \tag{1.1}$$

Where N/N_0 represents the proportion of photons which survive transport through a material of thickness x, and μ' represents the broad-beam polychromatic attenuation coefficient of the photons given their initial energy spectrum and the interaction cross sections of the material traversed (Attix, 2008). In an attenuation imaging system, an object is exposed to a field of X-rays. The spatial variation of the transmitted X-rays at the detector are used to generate an image.

In modern radiography, X-rays are produced by accelerating electrons into a rotating tungsten anode, wherein their kinetic energy is converted into heat, bremsstrahlung radiation, and characteristic X-rays (Bushberg *et al.*, 2011). The photon beam is then filtered to remove low-energy X-rays and reduce patient dose. This hardened beam is collimated, then passes through the patient and intercepts a flat-panel digital detector for imaging. For chest imaging, the X-ray tube typically operates at 500-800 mA and 120 kV. The high voltage allows visualization of the heart and lungs with reduced conspicuity of the ribs.

In CT, the X-rays are transported through the patient over multiple angles to reconstruct the position and attenuation coefficients of the patient's tissues. This process is repeated in slices in the axial direction to create a 3D visualization of the region of interest. Each voxel in a digitally reconstructed radiograph is represented by a value called a Hounsfield unit (HU), a measure of its attenuation coefficient. Modern CT scanners generate the 3D image data using iterative reconstruction methods, and simultaneously acquire multiple slices using cone-beam geometry and multiple-detector arrays. Slip ring electronics facilitate helical acquisition, reducing scan time to a few seconds. The motion of the gantry in a helical acquisition is quantified by its pitch, which is defined as

$$pitch = F_{table}/nT, \tag{1.2}$$

where F_{table} represents the axial distance traversed by the table in a single gantry rotation, n represents the number of rows in the detector array, and T represents the width of each row.

1.3.2. Talbot-Lau X-Ray Interferometry

X-ray interferometry uses the wave-optical properties of X-rays, rather than attenuation, to produce an image. In the Talbot-Lau setup, three diffraction gratings are placed in the beamline, labeled G0, G1, and G2. The G0 source grating effectively turns the large focal spot inside an X-ray tube into a coherent series of repeating line sources (Pfeiffer *et al.*, 2009). The passage of the beam through the G1 phase grating creates a diffraction pattern called the Talbot carpet, which varies with the distance from G1. This creates a specific fringe pattern at the plane of the G2 analyzer grating. The highly attenuating lines in the

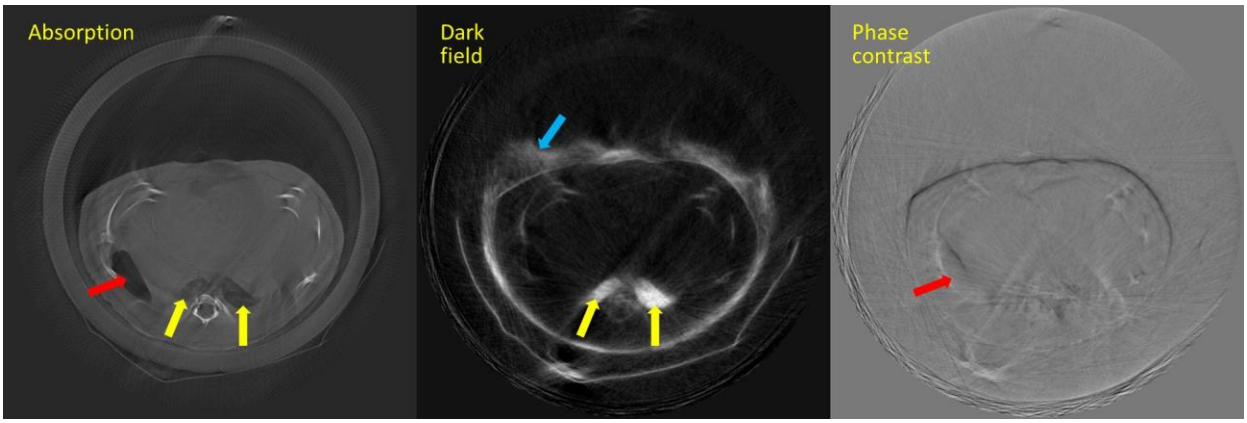

Figure 1.1. CT absorption, dark field, and phase contrast images of the same slice of a mouse. Red arrows indicate an air pocket visible in the absorption and phase contrast images. Yellow arrows indicate the lungs, visible in the absorption and dark field images. The blue arrow indicates the fur, only visible in the dark field image.

G2 grating are matched to this pattern, which allows the detector to separate the diffraction pattern generated by G1 from that generated by the object as the X-ray beam passes through it. Either G2 or the detector make small steps perpendicular to the direction of the beam, scanning the Talbot carpet across the detector. This allows the detection of small-angle scatter and the generation of a dark field image in which each pixel corresponds to the object's scattering power. As shown in Figure 1.1, tissues which are rich in microscopic density fluctuations, such as lung, have greater scattering power and can be imaged with high dark field contrast. Finer resolution than the detector pixel size is achievable in these images (Franz Pfeiffer *et al.*, 2008; Bech *et al.*, 2013).

Multiple preclinical TLXI prototypes are in development worldwide. Willer *et al.* (2021) have developed a dark field TLXI chest radiography unit. This device delivers a measured equivalent dose per scan that is a factor of 100 lower than that from a thoracic CT scan. However, Willer's radiography system suffers from an unacceptably large footprint and imaging artifacts due to instrument instability (Pfeiffer, 2019). Viermetz *et*

al. (2022) have developed a dark field TLXI CT system which has successfully imaged an anthropomorphic phantom. However, this system lacks a bow tie filter, resulting in capping artifacts and patient dose that is higher than necessary (Cao *et al.*, 2020). Benchtop TLXI systems for breast cancer histology have been developed by several groups, which can detect calcifications on the order of a few microns in excised samples (Michel et al., 2013; Scherer, Braig, et al., 2016; Willner *et al.*, 2014). There are currently no *in vivo* mammography systems in clinical use (Vignero, 2018).

In the context of medical imaging, total source-to-detector distance should be between 120-180 centimeters to maintain an acceptable footprint. It is also necessary to maintain a small object-to-detector distance to keep the expensive grating components to a reasonable size. Placing the G1 grating upstream of the patient reduces this distance. In grating design, it is important to consider where the G1 grating sits relative to the patient. An upstream G1 grating will more closely resemble the patterning of the G0 grating, whereas a downstream G1 grating will more resemble G2.

1.3.3. Finite Element Stress Analysis

The finite element method allows predictions to be made about the behavior of large bodies by dividing them into a mesh of small elements (Zienkiewicz *et al.*, 2005). Elements are discrete volumes defined by linked nodes, commonly tetrahedral or hexahedral. In finite element stress analysis (FEA), an assembly of segmented parts is meshed and placed under a load, whereupon the resulting stress and strain are calculated at each node. Hooke's law defines the relationship between stress and strain, which is quantified by the

Young's modulus of a given material (Hopcroft *et al.*, 2010). Young's Modulus is defined as

$$E = \frac{\sigma}{\epsilon}, \tag{1.3}$$

where E is Young's Modulus, σ is the force per unit area, and ϵ is the proportional deformation of the linkage between nodes. As an object deforms under load, the resulting change in shape is defined by Poisson's ratio, the ratio of the change in length in the transverse direction to the change in length in the axial direction. Given Young's modulus and Poisson's ratio, specialized software can solve the large system of equations necessary to perform FEA and assess the integrity of a structure.

Chapter 2. Materials & Methods

2.1. Simulation Software

2.1.1. GEANT4/TOPAS

GEANT4 is a C++ based 3D Monte Carlo particle transport toolkit. It tracks the motion of primary particles through a simulated geometry, accounting for material-specific particle interactions and external electromagnetic effects, then stores event and trajectory data for visualization and analysis. Modular lists of physics processes allow a user to reduce computational load by only considering particle behaviors specific to their needs (Agostinelli *et al.*, 2003). GEANT4's physics lists are exhaustive and regularly updated (GEANT Collaboration *et al.*, 2016).

The user must create all volumes in the geometry, assigning dimensions and materials. Materials can either be user-created or sourced from a National Institute of Standards and Technology (NIST) database embedded in GEANT4. The user must place each volume within the world, avoiding overlap. Sensitive volumes are then denoted for the storage of event information. The user must also specify the spatial, numerical, and energy distributions of the incident radiation, as well as the radiation type. The particle distribution characteristics may be input discretely or randomly sampled from a user-generated probability histogram. Finally, a physics list must be selected from GEANT4's repository (Geant Collaboration *et al.*, 2019).

The TOol for PArticle Simulation (TOPAS; version 3.7, TOPAS MC Inc., Menlo Park, CA, USA) is a software environment built around GEANT4 which specializes GEANT4's capabilities for medical physics applications (Faddegon *et al.*, 2020). TOPAS

simplifies the design of geometry and time features, as well as the use of Digital Imaging and Communication in Medicine (DICOM) images to supply patient geometry. A stack of DICOM images comprising the patient information is interpreted by an HU-to-material conversion table embedded in TOPAS to generate a patient volume. Each voxel in the patient volume is assigned density and elemental mass fraction values corresponding to its HU value in the input DICOM stack (Schneider *et al.*, 2000). The density conversion values are summarized in Figure 2.1. Simulation parameters are sourced from a modular file tree to ease troubleshooting and customization. A simulation can be initiated from any level of the file tree with downstream modules enabled or disabled as desired. An example of our TLXI file tree hierarchy is shown on Figure 2.2.

2.1.2. SpekCalc

SpekCalc (Version 1, Montreal, CA) is a tool for predicting the energy fluence spectrum emitted from an X-ray tube's tungsten anode. SpekCalc estimates the probability of electron survival at a given anode depth using a Monte Carlo-determined joint frequency density function,

$$f(u,x) = \eta_F(x)P_F(u|x) + \eta_M(x)P_M(u|x), \tag{2.1}$$

where η describes the frequency with which electrons reach depth x and P describes the probability of an electron at depth x retaining the fraction of its initial kinetic energy u (G. G. Poludniowski and Evans, 2007). Subscripts denote the separate contributions of electrons making their first pass (F) and subsequent passes caused by multiple scattering (M). The joint frequency density function has been pre-calculated over the range 40-300 kVp using the Monte Carlo code BEAMnrc.

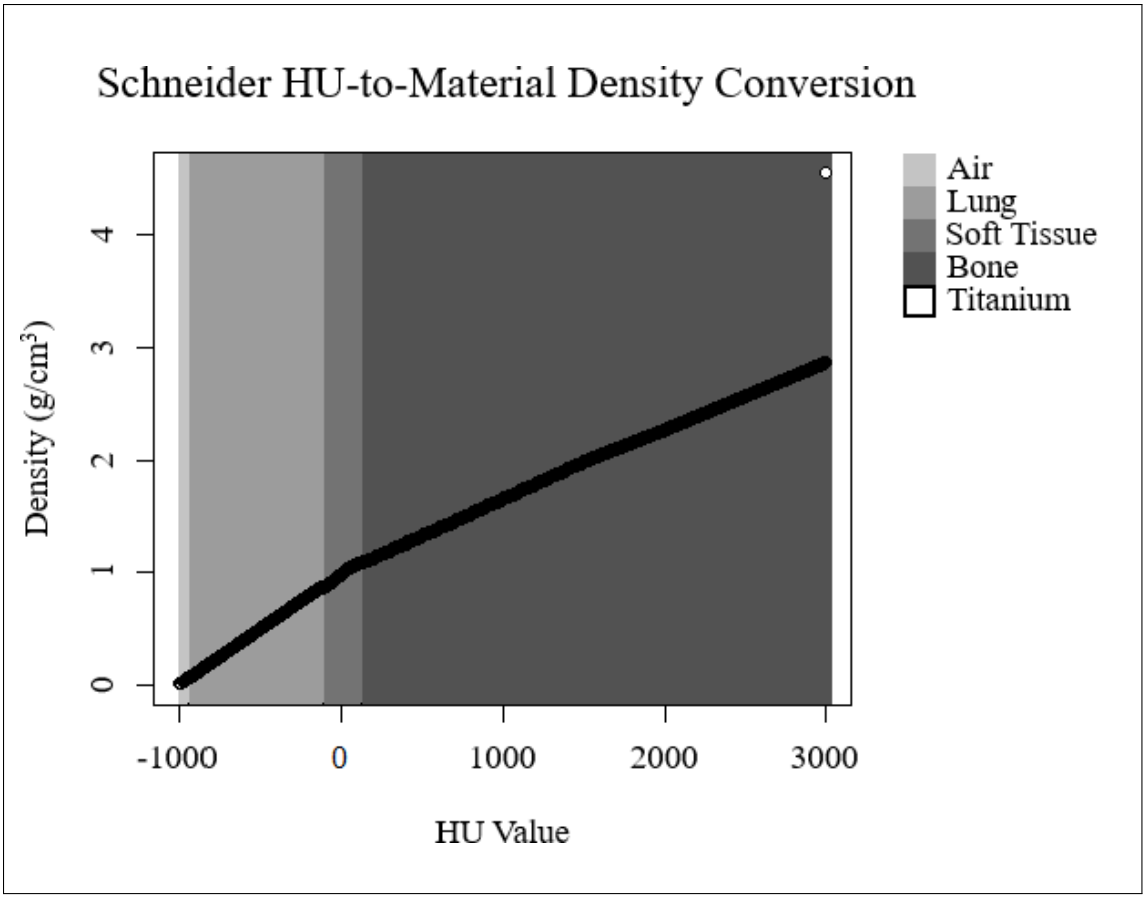

Figure 2.1. Scatterplot demonstrating the relationship between input DICOM HU values and output material density values in the TOPAS patient volume (Schneider *et al.*, 2000). The shaded regions indicate divisions in tissue type, where HU values between -1000 and -950 correspond to air, values between -949 and -120 correspond to lung, values between -119 and 120 correspond to soft tissue, values between 121 and 2994 correspond to bone, and 2995 corresponds to titanium.

From input tube potential, anode take-off angle, filtration material, and filtration thickness, SpekCalc determines the joint frequency density function, the resulting spectrum of bremsstrahlung and characteristic X-rays, and the photon attenuation by the filter and the anode itself (G. Poludniowski *et al.*, 2009). It outputs a histogram of the final energy fluence spectrum exiting the filter. Attenuation calculations from first principles have been validated against experimental data and shown to meet or exceed the predictions of older semi-empirical methods (G. G. Poludniowski, 2007).

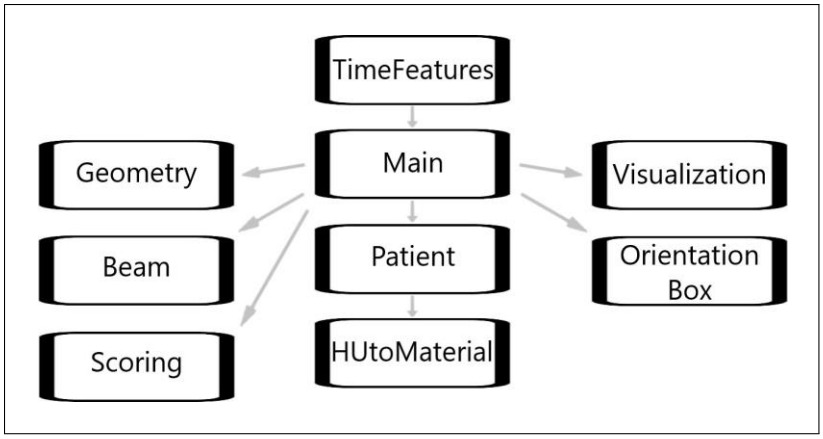

Figure 2.2. Hierarchy of simulation parameter files. The TimeFeatures module contains information for scanner motion during acquisition, as well as the number of histories run at each beam position. The Main module serves as the point of control for the user to include or exclude lower modules. It also defines basic parameters such the beam position and the world volume. The Beam module contains the probability distribution of the continuous x-ray spectrum – a histogram of photon energy weights generated via SpekCalc. The Geometry module contains position and material information for grating and shield components. The Visualization module defines options for the position and appearance of the graphical user interface. The Scoring module specifies the particle track data measured at scoring volumes for output files, such as energy deposition and particle fluence. The OrientationBox module defines basic geometry tools useful for setting up the simulation environment. The Patient module converts DICOM information into a voxelized volume using the included HUtoMaterial module. The simulation can be run from the level of the TimeFeatures or Main module, and all downstream modules can be enabled or disabled as needed.

2.1.3. Abaqus

Abaqus is a finite element platform for structural and heat transfer analysis (Börgesson, 1996). It allows FEA users to design and assemble individual parts of a structure in two or three dimensions, draw coordinate systems, create materials, assign part constraints and boundary conditions, define part interactions and contact mechanisms, create loads, mesh parts, visualize load interactions, and output field reports. pre-processing, analysis, and post-processing can be performed in a computer-aided engineering graphical user interface.

2.2. Application Design

2.2.1. Radiography Unit

This lab has previously designed and constructed a benchtop TLXI system for small animal imaging that has been used to visualize brown fat reserves in mice (Jacobs, 2020). We scaled and refined this design for human chest radiography and created an abstracted representation of the device geometry using TOPAS, shown in Figure 2.3. The geometry consists of an X-ray source, the diffraction gratings (G0, G1, and G2), stationary lead shields, mobile lead collimators, and a voxelized patient volume. To allow future users to experiment with different grating designs and device footprints, we have created multiple configurations, defined in Table 2.1.

As shown in Figure 2.3, all three gratings are positioned orthogonal to the beam axis. A voxelized CT scan of the Alderson RANDO phantom (Radiology Support Devices, Inc.; model 801, Long Beach, CA, USA) has been positioned so that its anterior aspect faces the upstream surface of the G2 grating. The distal (downstream) surface of the G2 grating is defined to be the detector plane, since the detector in a physical system will sit just behind the G2 grating. We refer to the number of photons which pass through this surface as the detector count. We used SpekCalc to compute the photon energy spectrum of a 120 kVp beam passing through 1 mm Al and 1 mm Cu filtration, resulting in a hardened beam with an effective energy of 70.7 keV. This spectrum is intended to be appropriate for chest and should match the design energy of the gratings.

Grating component dimensions require that the imaging field be limited to six inches in height. Rather than acquiring the entire chest at once, a scan begins with the

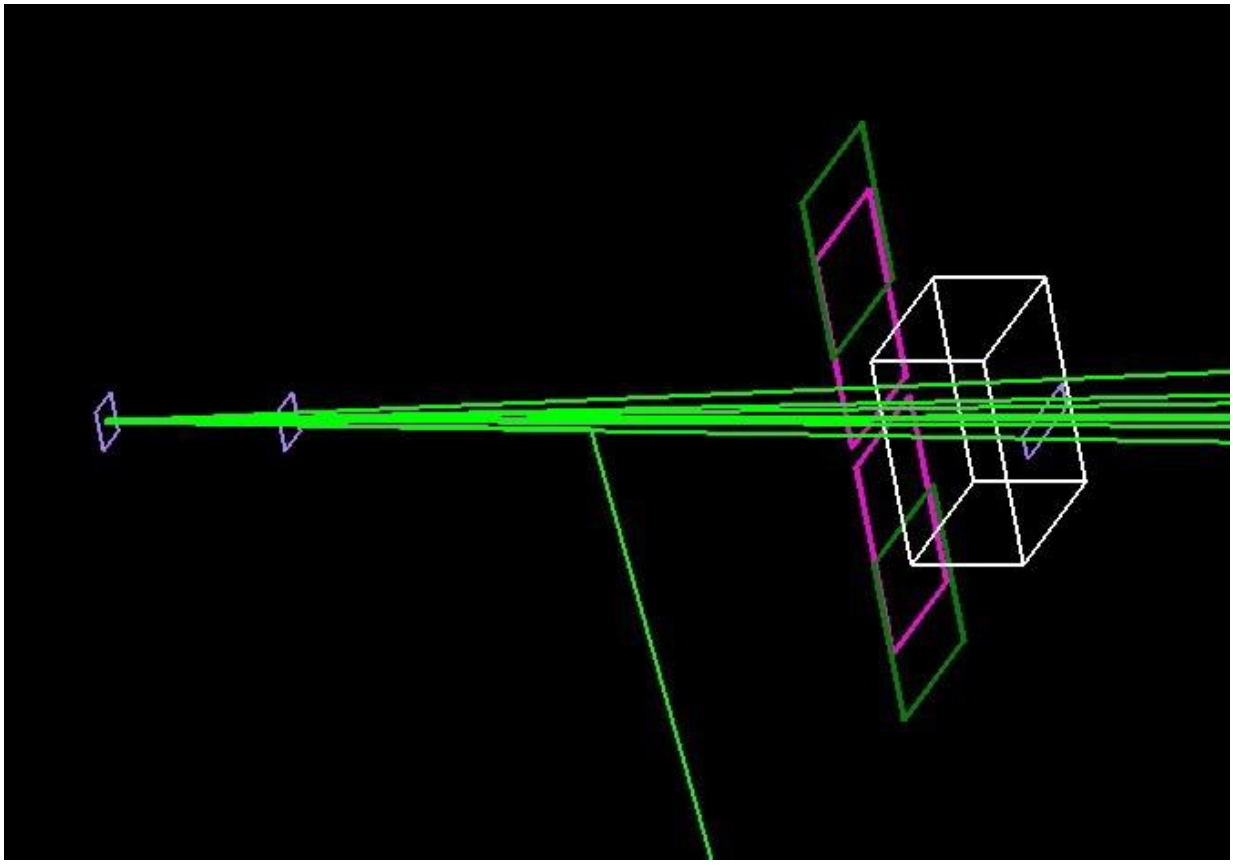

Figure 2.3. Visualization of the radiography unit geometry with 10 histories run at a single step. The bright green lines represent photon tracks originating from the source point on the left. To reach the detector plane, a photon must travel through the diffraction gratings, represented as light blue rectangles. Mobile collimators, shown in pink, are suspended from stationary lead shields, shown in dark green. The voxelized phantom geometry is represented by the white box.

Table 2.1. Grating positioning along the beam axis for different test setups. The beam source is positioned a short distance upstream of the G0 grating. The phantom is moved relatively closer to the beam source in the 150 cm setup so that the G2 grating does not collide with the phantom volume at the beginning and end of its rotation. *All testing was performed using this configuration.

Setup	Position (*cm*)					
	Source	G0	G1	G2	Phantom	Collimator
232 cm*	-45.4	-45	0	187	170.6	146.5
200 cm	-45.4	-45	0	155	138.6	114.5
180 cm	-45.4	-45	0	135	118.6	94.5
150 cm	-45.4	-45	0	105	87.6	64.5

optics tilted so that the bottom edge of the beam abuts with the top of the phantom's lungs. Between beam-on times, the optics pivot in small increments about an axis centered on the G1 grating until the top edge of the beam abuts with the bottom of the phantom's lungs. At each position, the beam emits a user-specified number of photons before rotating to the next position. Collimators positioned between G1 and the phantom translate with the beam to maintain a 6 cm projection at the detector plane. To compensate for variation in human lung height (average adult lung height is 35 cm), we added an additional margin of 6 cm to the scan length (Patwa *et al.*, 2015). We expect the motorized components of the radiography unit to be able to rotate the beam and optical components through the full scan arc over the course of about six seconds.

To simulate gratings with a 50% duty cycle, we have created unique materials in TOPAS which approximate a uniform 50-50 mixture of air and metal. The component mass fractions of each material are shown on Table 2.2. With this approach, we assumed that the entire beam interacts with a low-density metal sheet at each grating rather than alternating lines of air and high-density metal. G0 and G2 thicknesses were selected so that a 70.7 keV beam would be attenuated by 95% after passing through the bars of a patterned grating. This would allow 52.5% total transmission. Modeling the grating as a homogeneous slab, we expect the beam to transmit 22% from by-hand calculations. This causes the final simulated beam to have a different energy spectrum and spatial distribution than it would in practice. However, this simplification is necessary given that the grating patterning is too fine to feasibly replicate in a TOPAS geometry. Final grating thicknesses were 592 μm for G0, 200 μm for G1, and 661 μm for G2.

Table 2.2. Mass fractions of the component materials for each diffraction grating.

Grating	Elemental Weight						
	% Si	% Au	% Gd	% C	% N	% O	% Ar
G0	0	99.99	0	7.741E-7	0.004714	0.001447	8.007E-5
G1	99.95	0	0	6.409E-6	0.03904	0.01198	6.629E-4
G2	0	0	86.74	2.113E-6	0.01287	13.24	2.186E-4

We modified the Alderson RANDO phantom DICOM stack via Matlab (MathWorks; version R2021b, Natick, MA, USA) to reduce computation time and accommodate realistic scan conditions. Helical acquisition caused a hazing artifact to occur in slices that overlapped with air gaps between segments of the phantom. An example of this is shown in Figure 2.4. Downsampling by half in all three dimensions to reduce the severity of the helical overlap artifact, as well as the file size. Excess air volume was removed so the phantom can be positioned closer to the detector plane. The imaging couch was also removed, allowing the supine phantom to be represented in the upright position. Discontinuities within the phantom caused by support pegs and dosimeter cavities were painted over with the HU values of surrounding tissues to make the phantom volume more homogeneous. Extremely high and low HU values were redefined to cap values which fall within the HU-to-Material conversion table. The outcome of the phantom image processing steps is shown in Figure 2.5 and an example slice from the phantom volume in TOPAS is shown in Figure 2.6.

In TOPAS, all position, interaction, and energy deposition data for a given photon and its corresponding cascade of secondary particles are temporarily recorded in a structure referred to as a history. Information about a given history can be written to an output file before the history's data is purged at the beginning of the next history. We

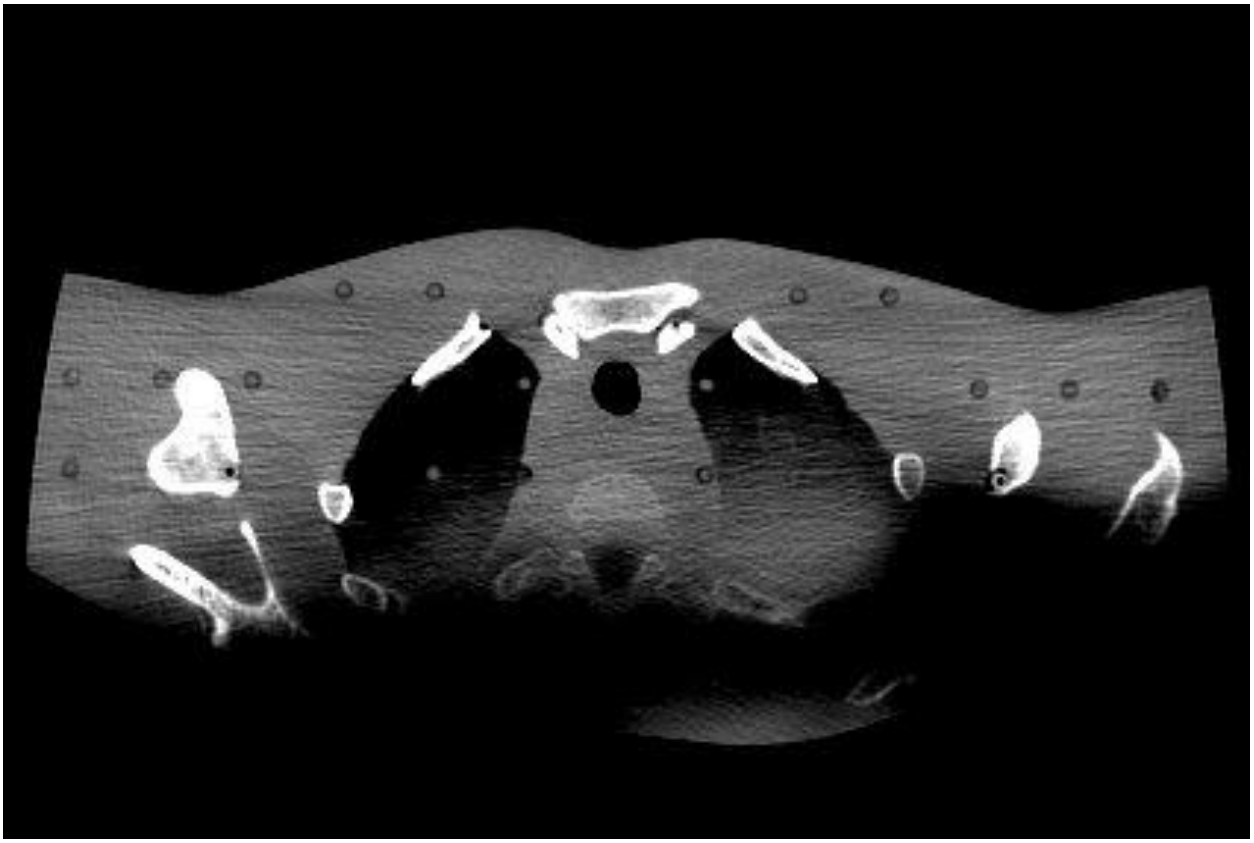

Figure 2.4. Example of the helical overlap artifact. The voxels within the darkened zone have HU values as low as -600, which TOPAS converts to lung tissue. Prior to downsampling, these values were in the range of -950 to -1000, which TOPAS converts to air.

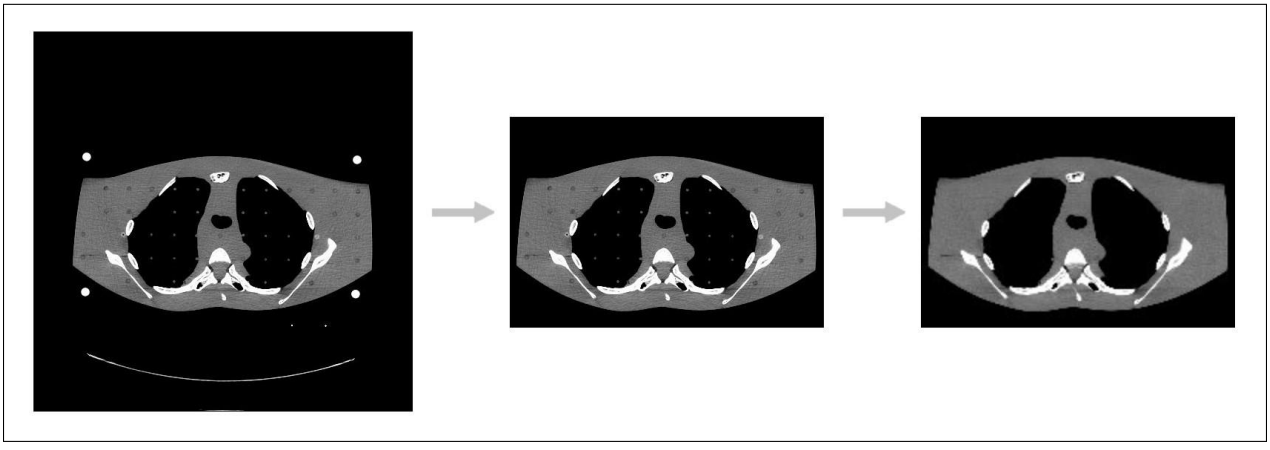

Figure 2.5. An example CT slice taken through the image processing procedure. Left: the original slice. Middle: the slice after removal of the couch and excess air. Right: the slice after HU value adjustments to remove non-anatomical discontinuities.

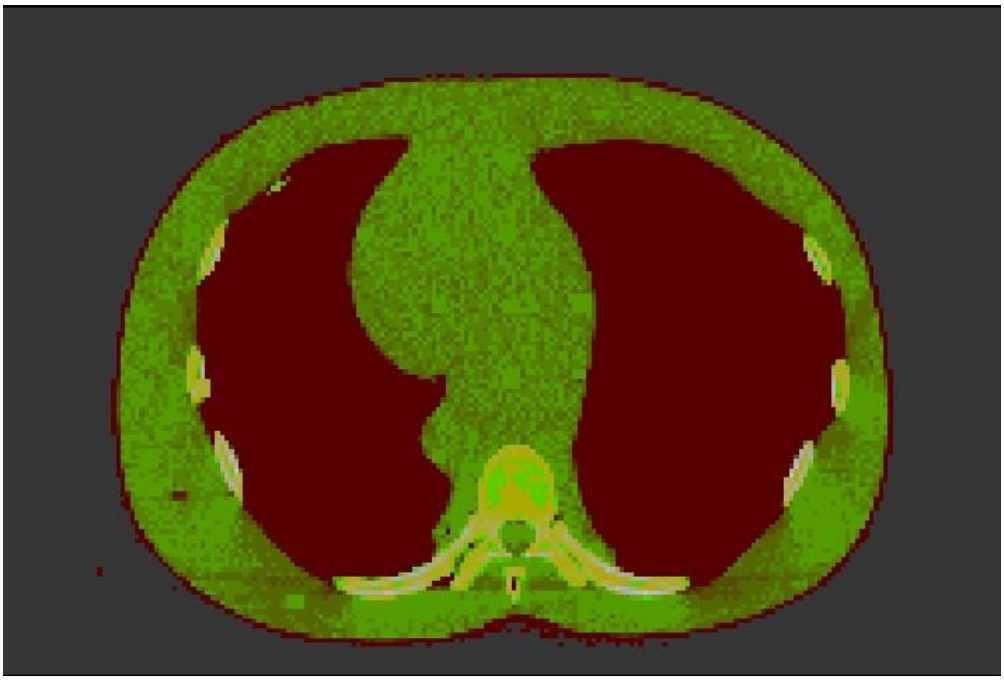

Figure 2.6. A slice of the processed phantom DICOM stack converted to a scoring volume in the TOPAS geometry. The HU-to-Material conversion table defines five materials: air, shown in grey; lung, shown in red; soft tissue, shown in green; bone, shown in white; and titanium, which is not shown. Each material except titanium corresponds to a bracket of HU values, defined by the least dense and most dense composition that material can have. Divisions within a material's bracket represent a linear interpolation between the minimum and maximum density (Schneider *et al.*, 2000).

have designated the voxelized phantom and each grating as scoring components, which record the following history data: the total number of primary photons that pass through the downstream surface of each grating, the energy deposited at each voxel within the phantom volume, and the dose scored at each voxel in the phantom volume. Grating metrics allow the comparison of image quality between different setup geometries, while phantom metrics allow comparison of dosimetry. To normalize results, users can run a simulation with the grating volumes disabled and determine the detector count when the average phantom dose reaches 0.1 mGy, the typical dose from a chest radiograph

(Thurston, 2010). This can be considered the benchmark photon count required to reach comparable image quality to a traditional chest scan.

To calculate meaningful dose metrics, we segmented the phantom into four material regions (ImageJ; version 1.53k, National Institute of Health, Bethesda, MD, USA). We have thresholded the input DICOM stack according to HU values from the HU-to-material conversion table, resulting in binary images containing information for one of four material types: air, lung, soft tissue, and bone. Examples of these single-material images are shown in Figure 2.7. The total energy deposited in each material was determined by multiplying the thresholded image stacks by the output energy deposition DICOM stack. The dose delivered to each material type was then calculated by dividing the material's energy deposition by its respective mass. For a measure of whole-body dose, we divided the total energy deposition by the total phantom mass, excluding the contribution of air. Material masses were calculated using densities found on the RANDO phantom's tech sheet, available at https://rsdphantoms.com/wp-content/uploads/2021/02/TECH-SHEET-ART-Phantom.pdf. The densities of cortical and trabecular bone have been averaged to a single value of 1.178 g/cm^3 for our calculations. This assumes that the bone distribution present within the simulated section of phantom is consistent with the average human body, with about 80% cortical bone and 20% trabecular bone (Morgan *et al.*, 2013).

2.2.2. Computed Tomography Unit

We modified the radiography unit geometry to include a CT couch and bow tie filter, shown in Figure 2.8. As per the recommendations of medical physics staff at Mary Bird Perkins Cancer Center, we modeled the CT couch as a 2 mm thick carbon fiber shell with

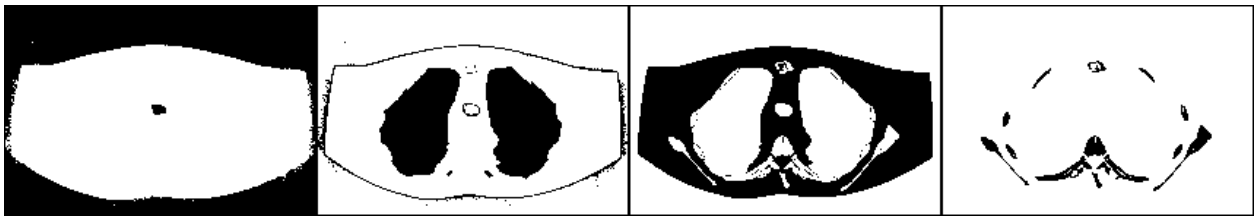

Figure 2.7. Thresholded slices from the input DICOM stack which contain only a single material. From left to right: air, lung, soft tissue, and bone. Black voxels have a value of 1 and white voxels have a value of 0. By multiplying these images by the output energy DICOM stack, material types can be isolated for dose calculations.

a low-density foam core (Neck, 2021). The couch is positioned so that its top surface is barely in contact with the voxelized phantom volume. The shape of the G2 grating has been modified to resemble the curved configuration seen in Figure 2.9, represented as a section of a cylinder with a radius equal to the distance between the grating and the beam source. With this geometry, all primary particles travel the same distance to reach the G2 grating. However, this is likely a simplification of the final device design, in which the G2 grating may be discretized into 13 cm flat subunits to conform with the model of flat-panel detector planned for use in a prototype device. Multiple arrangements, defined in Table 2.3, have been created for experimentation with optics positioning (Strobl, 2014).

Table 2.3. Grating positioning along the beam axis for different test setups. The beam source is positioned a short distance behind the G0 grating. The bow tie filter is positioned as close to the beam source as possible to reduce the effect of beam spread and thereby minimize the required materials. *All testing was performed using this configuration.

Setup	Position (*cm*)					
	Source	G0	G1	G2	Phantom	Bow Tie Filter
100 cm*	-59.4	-59	-41	41	0	-56.4
120 cm	-69.9	-69.5	-50.5	50.5	0	-66.9
150 cm	-85.4	-85	-65	65	0	-82.4
170 cm	-95.4	-95	-75	75	0	-92.4
200 cm	-110.4	-110	-90	90	0	-107.4

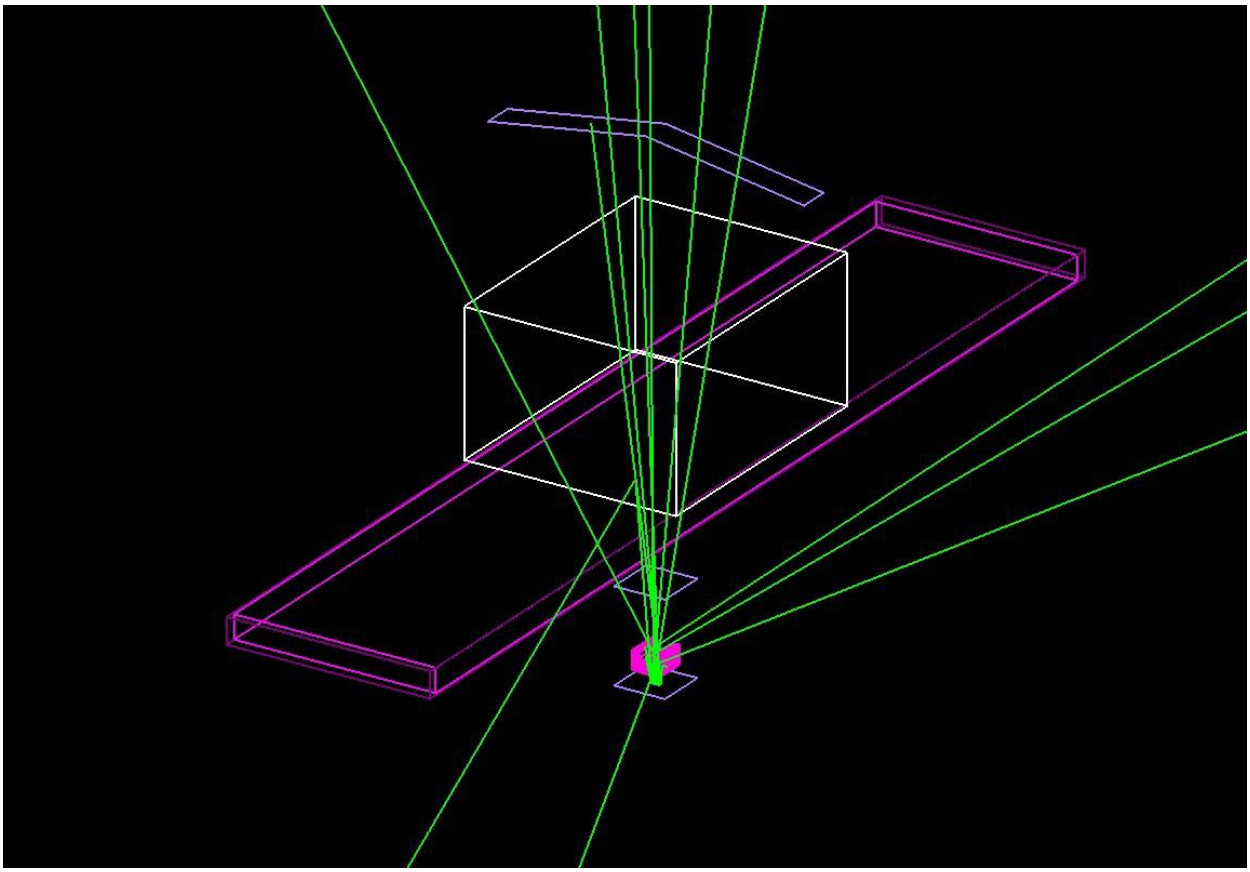

Figure 2.8. Visualization of the CT geometry with 20 histories run at a single step. The bright green lines represent photon tracks originating from the source point on the bottom. To reach the detector plane, a photon must travel through the diffraction gratings, represented as light blue rectangles. The bow tie filter, shown in pink, attenuates the edges of the beam to equalize detector signal. The voxelized phantom geometry is represented by the white box positioned on top of the purple imaging couch.

The geometry of the bow tie filter was based on the work of Yang *et al.* (2019). We used aluminum thickness values measured with a 120 kVp beam on the GE Revolution scanner's large filter. From the oblique aluminum thicknesses reported by Yang *et al.*, we modeled the bow tie filter volume as 22 discrete aluminum blocks, each spanning 2 degrees of the beam angle. A detailed view of the filter is shown on Figure 2.10.

We modified the methodology of Carver *et al.* (2015) for detector motion. Between beam-on times, the source and gratings rotate and shift about an axis centered on the

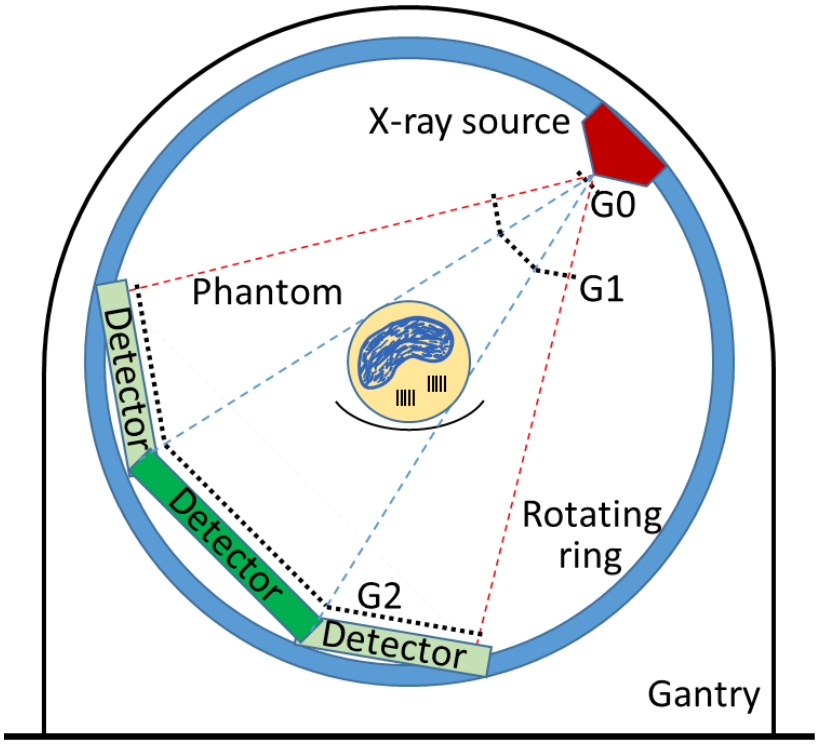

Figure 2.9. Illustration of CT prototype, showing key features of source, optics, and detectors.

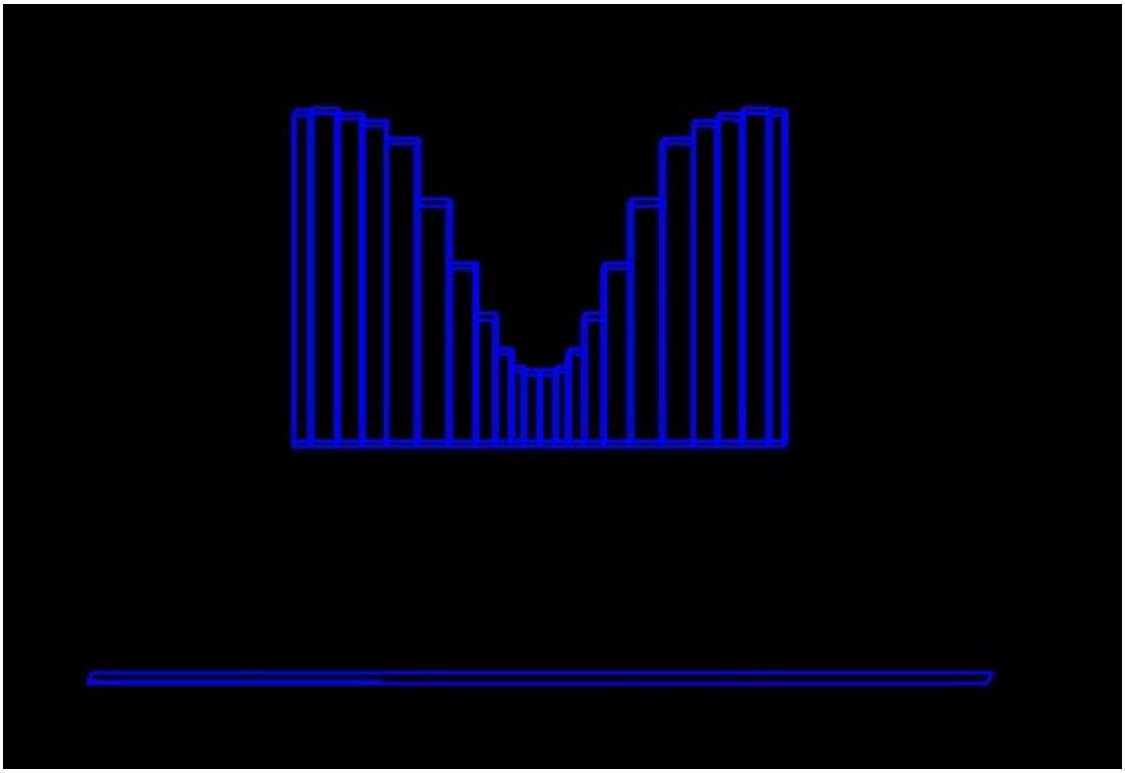

Figure 2.10. Detailed view of bow tie filter and Go grating.

phantom by an angle and axial distance determined from the pitch of the acquisition protocol. Scoring metrics and methods are the same as described in Section 2.2.1. For a normalization scan, users may set pitch equal to 1.0 and determine the number of histories necessary to bring the phantom's total dose to 7 mGy upon completion of the scan. The resulting detector count can be considered representative of a quality scan (Thurston, 2010).

2.2.3. Finite Element Analysis

We created a static model database in Abaqus which simulates a single diffraction grating placed under the rotational forces of a spinning CT gantry. The database contains schematics for each diffraction grating as well as an aluminum frame using common values for the elastic properties of gold, silicon, gadolinium (III) oxide, and aluminum. The mechanical and elastic properties of the simulation components are summarized in Table 2.4. Since the grating's line pattern is too fine to model in Abaqus, we adjusted the properties of the grating materials to approximate homogeneous slabs. Fritsch *et al.* and Miled *et al.* (2006; 2011) have shown that a 50% porous material can be represented as a homogeneous material with Young's modulus that is reduced by 75% of its original value. We approximated the 50% line duty cycle as equivalent to 50% porosity and reduced the Young's modulus of the grating materials accordingly.

The apparatus consisted of a grating positioned between two aluminum frames and surrounded on its edges by an aluminum inset, as shown in Figure 2.11. The inset prevents the grating from slipping. A static frictional force helps retain contact between the grating and frame. Static coefficient values between specific grating materials and

aluminum could not readily be found, but it is not necessary for the magnitude of the friction force to be perfectly realistic. We have chosen $\mu = 1.05$ for all gratings since it is a common coefficient for interfaces between metals. The edges of the grating have been fixed in the z-axis to prevent elements from intersecting with the frame under load.

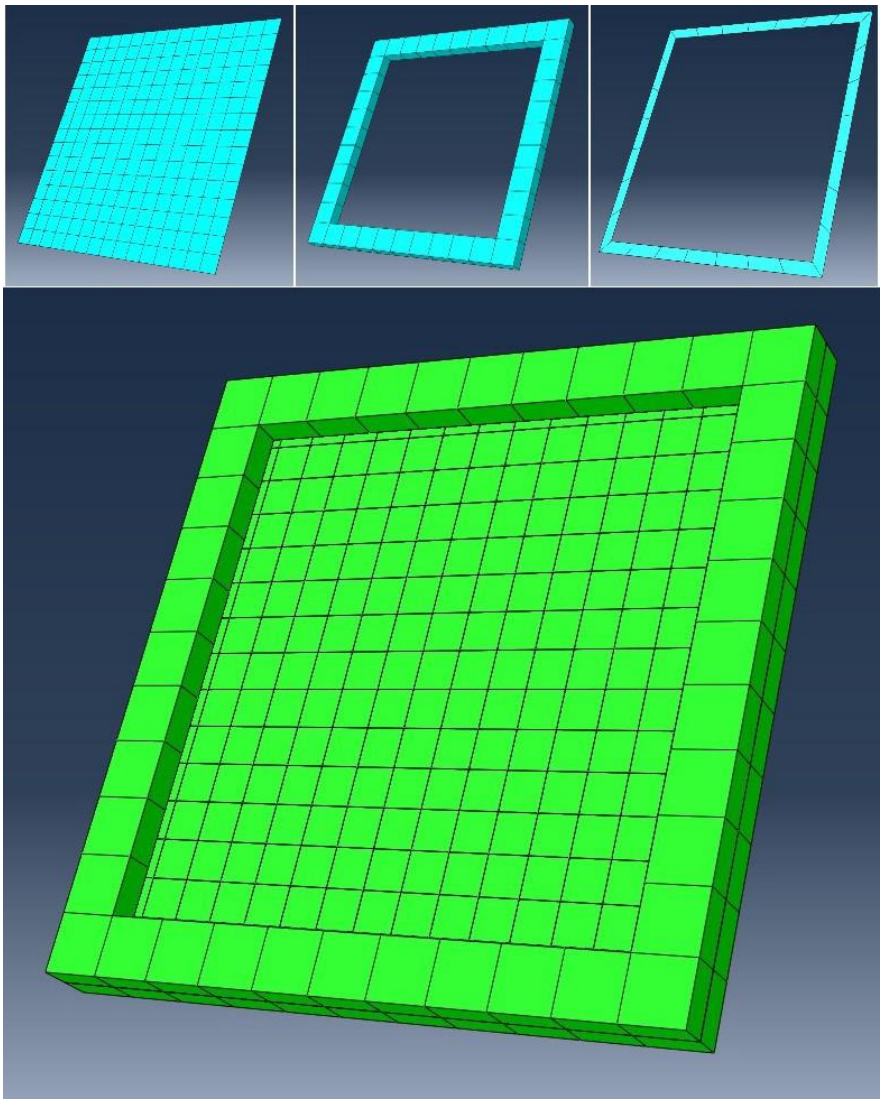

Figure 2.11. Top left: The diffraction grating; Top middle: The aluminum frame; Top right: The aluminum inset; Bottom: The assembled apparatus

To simplify force calculations, we assumed the gantry spins in uniform circular motion, that the weight of the grating is negligible relative to the centripetal force acting

on it, and that the distance from the center of rotation to the grating is the same across the entire surface of the grating. The outer surfaces of the frame are fixed in space so that the grating can deform against the inner surfaces of the frame while under the rotational force of the spinning gantry. A distributed load equal to

$$F = mr\omega^2 \tag{2.2}$$

is applied over the body of the grating, where m is the grating mass, r is the distance of the grating from the center of rotation, and ω is the maximum angular velocity of the gantry in radians per second. We calculated the rotational force acting upon each grating in a 6-second scan with a pitch of 1 and scanning length of 53 cm using the 100 cm CT setup defined in Table 2.3. We refer to this as the clinical load, which is included in Table 2.4. The load is applied over a ramp function, peaking at the maximum rotational force. We quantified deformation by measuring the maximum node displacement during loading.

Table 2.4. Mechanical properties of simulation components.

Component	Area ($cm \times cm$)	Density (g/cm^3)	Elastic Modulus (GPa)	Poisson's Ratio	Clinical Load (μN)
Frame	11	2.710	69	0.334	N/A
Inset	11	2.710	69	0.334	N/A
G0	10	9.650	55.5	0.42	135
G1	10	1.165	120	0.22	18.2
G2	10	3.5035	38.75	0.27	142

After completing a simulation job, Abaqus creates a field report of the displacement of each node which can be used to visualize and quantify optical component

deformation. We measure deformation by calculating the average displacement of the nodes surrounding the central element of the grating from field report data.

2.3. Testing

To ensure confidence in our applications, we subjected them to a series of test cases to verify that results match realistic expectations. All testing for the radiography application was performed with a 6-second scan using 100 time steps, which we judged to capture the scan dynamics with sufficient angular resolution (0.1448 degrees per step). Testing for the CT application was performed using 200 time steps and a pitch of 1, resulting a scanner rotation of 15.9 degrees per step over 8.8 rotations. The majority of the testing for the FEA application was performed with reference to the clinical load. The grating thicknesses used for FEA testing were assigned to unrealistically small values: 4.8 μm for G0, 7.7 μm for G1, and 20 μm for G2. These thinner gratings should be more flexible, so we expect simulation results to overestimate grating deformation.

2.3.1. Attenuation Test

Our first test determined whether beam attenuation by the grating volumes significantly increases patient dose in the radiography and CT applications. We compared the dose delivered to the phantom under three sets of simulation conditions: with all gratings enabled, with all gratings except G2 enabled, and with all gratings disabled. For configurations with disabled gratings, scoring planes were retained at the position where the downstream face of the grating would have been. We varied the number of histories run for each configuration so that the same photon count was reached at the detector plane. To determine the appropriate history count, we performed an initial set of

low-statistics trials (4,000,000 histories for each configuration). From our scoring metrics, we calculated the percent difference in the detector count between each configuration. For the radiography setup, we judged 80,000,000 histories to be sufficient to establish average behavior under the gratings-enabled configuration. Fewer photons were run in the setups with less attenuating material to achieve uniform detector count across all high-statistics trials: 22,670,700 histories for trials with all gratings enabled except the G2 grating and 2,205,100 histories for trials with all gratings disabled. For the CT setup, we ran 160,000,000 histories for the gratings-enabled configuration, 49,137,800 for the G2-disabled configuration, and 4,745,600 for the gratings-disabled configuration. This allowed us to compare dose between configurations given scans of the same image quality.

For each configuration, we extracted the scoring metrics after running the beam with the appropriate high-statistics history count. To establish average behavior, we repeated this process using a new random seed for a total of three trials per grating configuration. For each setup, we used the unpaired one-sided Student T-test to evaluate the difference in calculated phantom dose between configurations. The validation criteria were:

- there should be negligible difference between patient dose metrics for the gratings-disabled and G2-disabled configurations since adding material upstream of the patient does not require more photons to interact with the patient to match the detector count;
- patient dose metrics for the gratings-enabled configuration should be greater than those of the gratings-disabled configuration since there is more attenuating material downstream of the patient.

2.3.2. Material Conversion Test

Our second test determined whether the HU values of the input DICOM stack are appropriately converted to phantom volume materials in the radiography and CT applications. To evaluate candidate materials individually, we manipulated the phantom DICOM stack via MATLAB to produce blocks of homogeneous material with HU values corresponding to air, soft tissue, and bone, according to the HU-to-material conversion table. We then created a second set of phantom blocks in which the material was assigned manually, rather than with a DICOM input. Trials were run with all gratings disabled to include only the effects of the phantom material on the beam.

We used the same method described in Section 2.3.1 to determine the history count for each run. For the radiography setup, 20,000,000 histories were run using both the DICOM-based and manually-assigned soft tissue phantom blocks. To match image quality, 303,200 histories were run for the air phantom blocks. We could not match image quality with the bone phantom blocks given our computational resources. Rather, high-statistics trials with the bone phantom blocks were run with 20,000,000 histories. For the CT setup, we ran 40,000,000 histories in each high-statistics trial for the soft tissue phantom blocks, 1,204,800 for air phantom blocks, and 40,000,000 for the bone phantom blocks.

We repeated high-statistics trials with new random seeds for a total of three trials per phantom block, extracting the scoring metrics after each trial. To establish average behavior, we repeated this process using a new random seed for a total of three trials per block. We used the unpaired one-sided Student T-test to evaluate the significance of the dose increase for denser blocks and the unpaired two-sided Student T-test to evaluate the

difference in calculated block dose between each manually-assigned block and its DICOM-generated counterpart. The validation criteria were:

- phantom block dose should be significantly lower in the air blocks than in the soft tissue blocks;
- soft tissue block dose should be significantly lower than bone block dose when the measured bone block dose is scaled up by the detector count
- the dose measured for each manually-assigned block should not be significantly different from its DICOM-generated counterpart.

2.3.3. Hand Calculations

To determine whether the grating and phantom materials appropriately attenuate the X-ray beam, we performed two additional sets of simulations in which all volumes were disabled. For the first set, a 1-millimeter-thick slab was placed at the G0 position. For the second set, we instead placed the phantom block at the G0 position. We modified the beam source to emit monochromatic 70.7 keV photons and extracted photon count at the downstream face of the block after running 20,000,000 histories. This was repeated three times to establish average behavior with each grating material assigned to the slab and each phantom material assigned to the block. We checked our results against narrow beam attenuation calculations including air attenuation and neglecting coherent scatter. Attenuation coefficients for each grating material were sourced from the NIST XCOM database (Berger *et al.*, 1999). Attenuation characteristics for these materials are summarized on Table 2.5. We used the two-sided Z-test to evaluate the difference in percent attenuation between the simulation gratings and our by-hand calculations. The validation criterion was that there should be negligible difference between the percent beam attenuation of the simulation results and by-hand calculations.

Table 2.5. Attenuation characteristics of each grating and phantom material for a 70.7 keV equivalent photon beam. Phantom block density is determined from the HU-to-material conversion table embedded in TOPAS using -999 HU for Air, 40 HU for Soft Tissue, and 2994 HU for Bone.

Attenuating Material	Mass Attenuation Coefficient (cm^2/g)	Thickness (cm)	Density (g/cm^3)
G0	2.619	0.1	9.650
G1	0.2267	0.1	1.1650
G2	6.465	0.1	3.5035
Air	0.1642	27.73	0.012436
Soft Tissue	0.1807	27.73	1.038591
Bone	0.2329	27.73	2.86676

2.3.4. Deformation Pattern Test

Our third test determined whether contact interactions prevent off-axis sliding in the FEA application. We tested for the appearance of a radially symmetric deformation pattern of the diffraction gratings during radially symmetric loads. We ran simulations in which the clinical load was applied as a distributed force across the body of the grating. From output field reports, we measured the displacement of four off-axis nodes with the same absolute coordinates, displayed in Figure 2.12. We repeated this process for multiple loads within two orders of magnitude of the clinical load to cover a large range of possible gantry rotation speeds. Symmetry was evaluated via outlier analysis, in which the z-score was calculated for each off-axis node. Simulations with no points having a z-score greater than one were considered passing. The validation criterion was that all simulations with loads within two orders of magnitude of the clinical load should pass.

2.3.5. Elastic Properties Test

Our fourth test determined whether the elastic properties of the diffraction gratings appropriately influenced deformation in the FEA application. We ran simulations in which

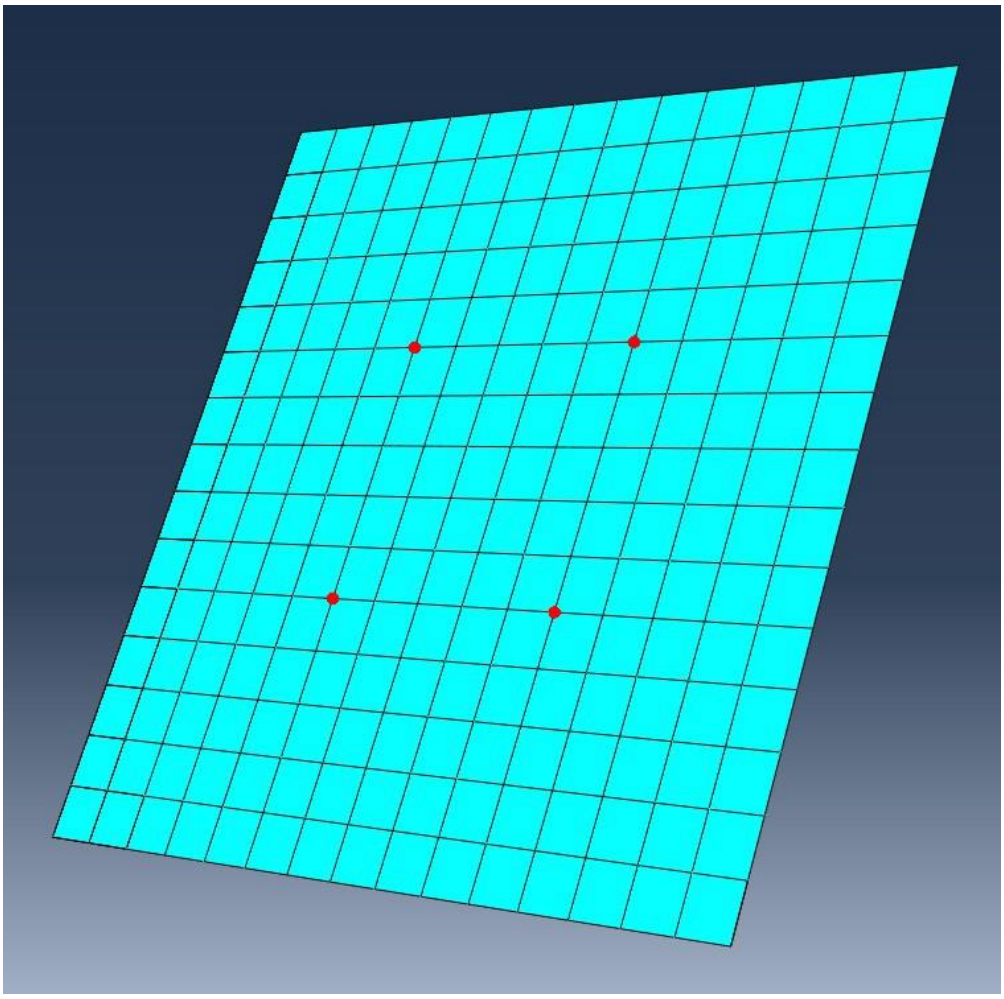

Figure 2.12. Example grating displaying off-axis nodes used for assessment of deformation pattern symmetry.

the clinical load was applied as a distributed force across the body of the grating, measuring the displacement of the central element as described in Section 2.2.3. We repeated this process, modifying the Young's modulus of the grating material to within two orders of magnitude of the base value. To linearize data as appropriate to Equation 1.3, we plotted central element displacement against the inverse of Young's Modulus. We fit the data with a least-squares regression line and evaluated correlation with a Pearson's r test. The validation criterion was that central element displacement

should be highly correlated with inverse Young's modulus, with a Pearson's r value greater than 0.95.

2.3.6. Load Distribution Test

Our last test determined whether our uniform approximation of the force distribution across the diffraction gratings in the FEA application was appropriate. We calculated the load applied to each grating when placed at various positions within 50 to 150% of the distance to the center of rotation used to calculate the clinical load. We ran simulations in which the load was either applied uniformly or nonuniformly - taking into consideration the variation in force across the grating. The nonuniform load was greater at the edges of the grating than at the midline because of the slightly greater distance from the center of rotation. The displacement of the central element and off-axis nodes was measured as described in Sections 2.2.3 and 2.3.4. The validation criterion was that displacement of the central element and off-axis nodes resulting from application of the nonuniform load should not be more than 5% different than that resulting from application of the uniform load.

Chapter 3. Results

3.1. Attenuation Test

We assessed the attenuation caused by the presence of the optical components in the beam. The results are summarized in Table 3.1, Table 3.2, and Figure 3.1. Statistical tests show that the whole body dose for the gratings-enabled configuration was significantly greater than that of the gratings-disabled configuration for both the radiography and CT setups ($p < 0.001$, $71.64 \pm 0.02\%$ difference for radiography; $p < 0.001$, $72.48 \pm 0.02\%$ difference for CT). While the whole-body dose for the G2-disabled configuration was significantly greater than that of the gratings-disabled configuration for the CT setup ($p < 0.001$, $10.22 \pm 0.09\%$), the radiography setup showed no significant dose difference ($p = 0.14$, $0.5 \pm 0.2\%$). The statistical difference in CT is due to the source-detector geometry in combination with beam hardening. Rotation of the beam around the phantom results in a large number of time points in which a fraction of the fan beam either passes through a smaller thickness of material or misses the phantom altogether before reaching the detector plane. Since a large proportion of low-energy photons are filtered out by the G1 grating, there is a smaller contribution to the detector count from the fraction of the beam which misses the phantom in the G2-disabled and gratings-enabled configurations. Normalizing by detector count results in a higher number of photons in the gratings-disabled setup which reach the detector without interacting with the patient, making detector count a poor indicator of matched image quality for the gratings-disabled configuration. The difference could be resolved by dynamically collimating the beam to match the phantom width at all angles of rotation. Omitting the

gratings-disabled CT data, these results confirm our expectation that patient dose is increased when attenuating material is added downstream of the patient, but not when it is added upstream of the patient. Our TOPAS applications have met validation criteria for attenuation behavior.

Table 3.1. A summary of the attenuation test results for the radiography setup. Uncertainties represent one standard deviation.

Setup	Beam Intensity (# of X-rays)				Whole Body Dose (*nSv*)
	Initial	G0	G1	G2	
Gratings Enabled	8E7	9.044E6 ±2E3	7.881E6 ±1E3	1.3767E5 ±6E1	1.4851 ±7E-4
G2 Disabled	2.26707E7	2.5629E6 ±7E2	2.233E6 ±1E3	1.382E5 ±2E2	4.190E-1 ±7E-4
Gratings Disabled	2.2051E6	2.20654E6 ±4E1	2.1866E6 ±2E2	1360E5 ±2E2	4.212E-1 ±2E-4

Table 3.2. A summary of the attenuation test results for the CT setup. Uncertainties represent one standard deviation.

Setup	Beam Intensity (# of X-rays)				Whole Body Dose (*nSv*)
	Initial	G0	G1	G2	
Gratings Enabled	1.6E8	1.9248E7 ±1E3	6.502E6 ±1E3	3.057E5 ±7E2	1.2410 ±5E-4
G2 Disabled	4.91378E7	5.911E6 ±2E3	1.9967E6 ±3E2	3.042E5 ±3E2	3.804E-1 ±3E-4
Gratings Disabled	4.7456E6	5.1660E6 ±5E2	1.8372E6 ±8E2	3.050E5 ±4E2	3.416E-1 ±1E-4

Detector count was successfully matched for all configurations. In the radiography setup, the most different detector counts were the G2-disabled and gratings-disabled configurations ($p < 0.001$, $1.6 \pm 0.2\%$ difference). We consider the difference to be negligible and attribute the low p-value to perfect counting efficiency in the Monte Carlo model, coupled with high-statistics runs. In the CT setup, there was a significant

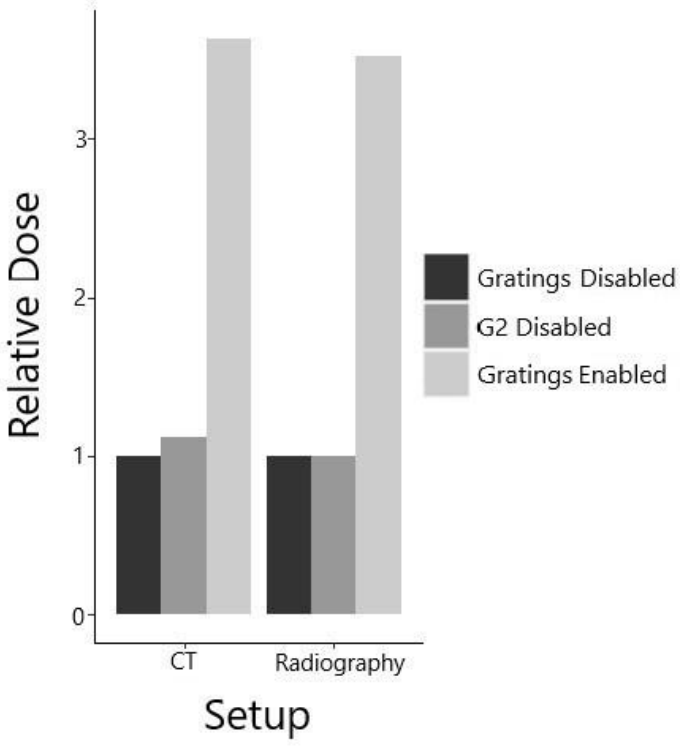

Figure 3.1. Plot of phantom whole body dose for each configuration normalized by the dose in the gratings-disabled configuration. Error bars are too small to visualize.

difference between the detector counts for gratings-enabled and G2-disabled configurations ($p = 0.049$, $0.5 \pm 0.2\%$ difference), which we consider negligible.

3.2. Material Conversion Test

We assessed the dose delivered to patient tissues. Results are summarized in Table 3.3, Table 3.4, and Figure 3.2. Statistical test results for the radiography setup show that the dose delivered to DICOM-generated and manually-assigned phantom blocks was approximately the same for each material, and that more dose was delivered to blocks composed of denser materials. No pair of blocks composed of the same material received significantly different doses except for the bone blocks ($p = 0.0155$). However, the difference was small ($0.012 \pm 0.005\%$). Significantly greater dose was delivered to the soft tissue blocks than to the air blocks ($p < 0.001$ for both; $5303 \pm 9\%$ difference for

DICOM-generated, 5300 ± 5% for manually-assigned). Scaling bone block dose proportionally by detector count, we can confirm that greater dose was delivered to the bone blocks than to the soft tissue blocks ($p < 0.001$ for both; 546600 ± 100% difference for DICOM generated, 541300 ± 100% for manually-assigned).

Table 3.3. A summary of the material conversion test results for the radiography setup. Setups labeled "DICOM" correspond to trials with DICOM-based phantom blocks. Setups labeled "Manual" correspond to trials with manually-assigned materials. Uncertainties represent one standard deviation.

Setup	Beam Intensity (# of X-rays)				Dose (*nSv*)
	Initial	G0	G1	G2	Phantom
DICOM Air	303200	303353 ±6	300570 ±30	188400 ±400	0.04305 ±0.00007
DICOM Soft Tissue	20000000	20013700 ±100	19834100 ±400	189800 ±200	2.3263 ±0.0005
DICOM Bone	20000000	20011800 ±100	19831000 ±400	18 ±9	1.18395 ±0.00004
Manual Air	303200	303353 ±6	300570 ±30	188400 ±400	0.04310 ±0.00004
Manual Soft Tissue	20000000	20013700 ±200	19834100 ±400	188000 ±200	2.3273 ±0.0004
Manual Bone	20000000	20011800 ±100	19831000 ±400	18 ±9	1.18409 ±0.00004

For the CT setup, the detector counts generally showed poor agreement, with the greatest difference being between the DICOM-generated and manually-assigned bone phantom blocks ($p < 0.001$, 19.3 ± 0.5% difference). We have omitted the CT results from statistical analysis due to inconsistencies caused by the CT sourced-detector geometry. We attribute this to the CT source-detector geometry. Rotation of the beam around the homogeneous phantom block results in a large number of time points in which a fraction of the CT beam either passes through a smaller thickness of material or misses the block altogether before interacting with the G2 grating. Since only a fraction of the beam is

Table 3.4. A summary of the material conversion test results for the CT setup. Setups labeled ”DICOM” correspond to trials with DICOM-based phantom blocks. Setups labeled ”Manual” correspond to trials with manually-assigned materials. Uncertainties represent one standard deviation.

Setup	Beam Intensity (# of X-rays)				Dose (*nSv*)
	Initial	G0	G1	G2	Phantom
DICOM Air	1204800	1310300 ±300	463600 ±600	344000 ±1000	0.0820 ±0.0006
DICOM Soft Tissue	40000000	43543900 ±900	15568000 ±2000	342000 ±500	1.7554 ±0.0002
DICOM Bone	40000000	43522000 ±1000	15487000 ±2000	222800 ±500	0.9525 ±0.0001
Manual Air	1204800	1310300 ±300	463600 ±600	344000 ±1000	0.0819 ±0.0006
Manual Soft Tissue	40000000	43543900 ±900	15569000 ±2000	383300 ±100	1.7491 ±0.0003
Manual Bone	40000000	43522000 ±1000	1548700 ±2000	266100 ±200	0.94899 ±0.00001

affected, detector count is not directly proportional to history count for phantoms of different compositions. Considering only the radiography results, the application meets validation criteria: input HU values are converted to the appropriate materials and coarse increases in HU values yield more attenuating materials.

The image quality matching technique was successful for achieving equal detector count for the air and soft tissue phantom blocks in the radiography setup. The largest detector count difference was between the DICOM-based and manually-assigned soft tissue blocks ($p < 0.001$, $0.9 \pm 0.1\%$), which we consider negligible. Detector count for the DICOM-based and manually-assigned bone blocks match exactly. For dose analysis, we use the ratio of the detector count for the bone block to the detector for the corresponding DICOM-based or manually assigned soft tissue block as a conversion factor to scale up the bone block dose.

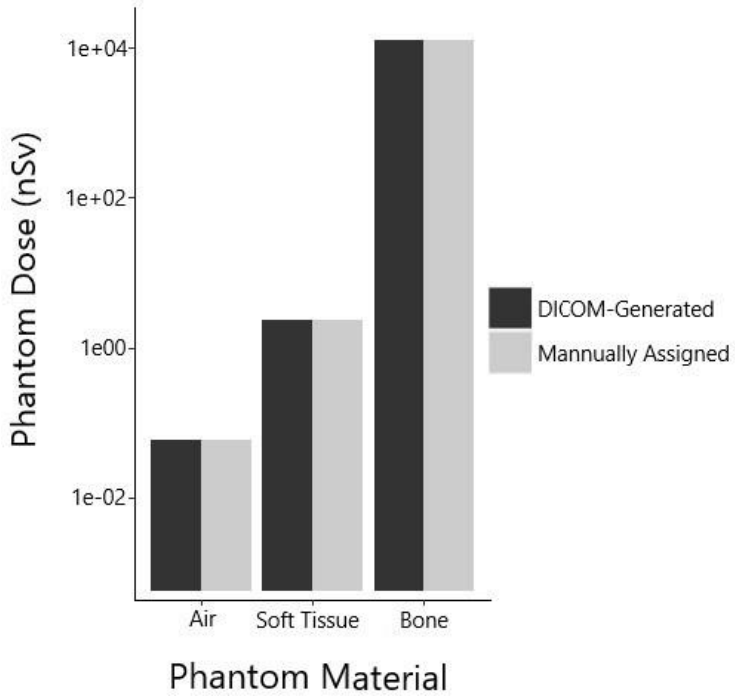

Figure 3.2. Plot of phantom block dose for each material type. Error bars are too small to visualize.

3.3. Hand Calculations

We compared simulation attenuation measurements to by-hand calculations. The results are summarized in Table 3.5 and Figure 3.3. Expected differences due to broad-beam effects are evident, but the trends across materials are comparable between simulation measurements and hand calculations. Statistical test results show negligible difference between simulation and hand beam transmission for silicon and both air blocks, but not for gold, Gd_2O_3, and the soft tissue blocks (34.3 ± 0.1% difference for Au, 1.333 ± 0.005% for Si, 7.85 ± 0.08% for Gd_2O_3, 0.4676 ± 0.0007% for the DICOM-based block air block, 0.461 ± 0.001% for the manually-assigned block air block, 33.0 ± 0.2% for the DICOM-based soft tissue block, 31.8 ± 0.3% for the manually-assigned soft tissue block). The history count was not high enough to get a quantitative measurement of the

proportion of photons transmitted through the bone blocks so they have been omitted from statistical analysis.

Table 3.5. Comparison of theoretical and simulated beam transmission for a 70.7 keV monochromatic beam traveling through 1-mm-thick slabs of each grating material and 27-cm-thick blocks of each phantom material. Uncertainty is propagated from the standard deviation of the photon count measurements.

Attenuating Material	Transmitted Beam		Traversed Thickness (cm)
	By-Hand (%)	Simulated (%)	
Au	5.649	7.584 ±0.008	0.1
Si	97.06	98.354 ±0.005	0.1
Gd_2O_3	9.599	10.353 ±0.008	0.1
DICOM Air	94.494	94.9359 ±0.0007	27.73
DICOM Soft Tissue	0.9737	1.295 ±0.002	27.73
DICOM Bone	9.078E-07	2E-6 ±3E-6	27.73
Manual Air	94.494	94.9297 ±0.009	27.73
Manual Soft Tissue	0.9737	1.284 ±0.003	27.73
Manual Bone	9.078E-07	2E-6 ±3E-6	27.73

We consider validation criteria to be met only for the silicon slab and the air blocks but are confident that the simulation materials behave properly. The difference between hand calculations and simulation measurements can be explained by scatter angle dynamics present in the simulations which were not accounted for in the hand calculations. Our photon-scoring volumes do not discriminate scattered photons from primary photons so the simulation environment is set up in broad-beam geometry criteria (Attix, 2008). Under these conditions, a small amount of coherently scatter photons are

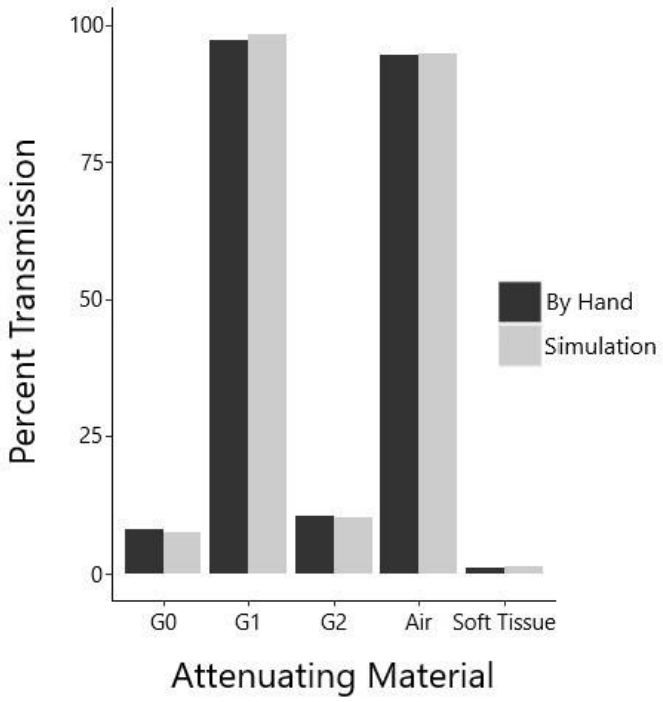

Figure 3.3. Plot of theoretical and simulated transmission data shown in Table 3.5. Bone has been omitted. Error bars are too small to visualize.

scattered at a large enough angle to miss the scoring surface, causing hand calculations to overestimate the number of transmitted photons. This effect is small, but more noticeable in the phantom block simulations, where the scoring surface represents a smaller solid angle at the upstream surface of the block. Additionally, some Compton scattered photons are scattered at a small enough angle to pass through the scoring surface, causing hand calculations to underestimate the number of transmitted photons. Photon Compton scatter angle for diagnostic energy beams is relatively isotropic so the overestimate can be quantified as approximately

$$f_c = (1 - e^{-\mu\rho x}) * \frac{\mu_C}{\mu} * \frac{A}{4\pi(\frac{x}{2})^2}, \tag{3.1}$$

where f_C represents the fraction of Compton scattered photons which intercept the scoring surface, μ represents the material's narrow beam attenuation coefficient, μ_C represents the material's Compton scatter cross section, ρ represents the material's density, and A represents the area of the scoring surface. This approximation considers the probability of Compton scatter to be equal in all directions, the center of the attenuating object to be the average position at which scatter occurs, and the area of the scoring surface to be representative of the solid angle from the center of the attenuating object.

3.4. Deformation Pattern Test

We determined whether contact interactions prevent off-axis sliding in the FEA application by measuring the displacement of off-axis nodes with equal absolute coordinates after applying a uniform loading to each grating. Results shown in Table 3.6 generally confirm that the grating volumes maintain contact with the frame volumes while under load. 20 of the 27 simulations showed passing symmetry, with the least symmetric deformation patterns observed on the G1 grating. The majority of failing simulations are qualitatively symmetric. The three most asymmetrically deformed gratings are shown alongside a symmetrically deformed grating in Figure 3.4. The asymmetric G1 deformations are likely attributable to a low load which failed to establish contact, as well as a correspondingly low friction force, which failed to prevent small misalignments. The G1 grating's clinical load has the lowest magnitude since the grating is the least massive and closer to the center of rotation than G0. The asymmetric pattern observed for the G2 grating at 100% clinical load is qualitatively identical to the symmetric pattern observed at other loads. We were able to impose symmetry for the G1 grating at 1000% clinical

Table 3.6. Highest z-score for the off-axis nodes in each simulation in the displacement pattern tests. Testing was performed for each grating with various loads within two orders of magnitude of the clinical load.

% Clinical Load	Maximum Z-Score		
	G0	G1	G2
1	0	1.16	0.976
5	0	1.11	0
10	0	01.07	0.948
50	0	1.50	1.006
100	0	0	1.50
500	0	0	0
1000	0	1.50	0
5000	0	0.866	0
10000	0	0	0

load and the G2 grating at 100% clinical load by applying a minuscule force to the gratings prior to loading. This step helps initiate contact and has negligible impact on displacement measurements in simulations which can initiate contact without it. The application has been modified to implement this contact step for all gratings. Overall, the application has met validation criteria. However, future users should check for grating symmetry when applying loads on the order of 10^{-7} N.

Additionally, we have quantified the relationship between the magnitude of the uniform body load and the off-axis node displacement for each grating as shown in Figure 3.5. Results confirm that grating deformation obeys Hooke's law for a range of loads near the clinical load, with Pearson's r coefficients exceeding 0.9 for all three gratings.

3.5. Elastic Properties Test

We quantified the relationship between the Young's Modulus and the deformability of the gratings in the FEA application by modifying each grating's Young's Modulus and

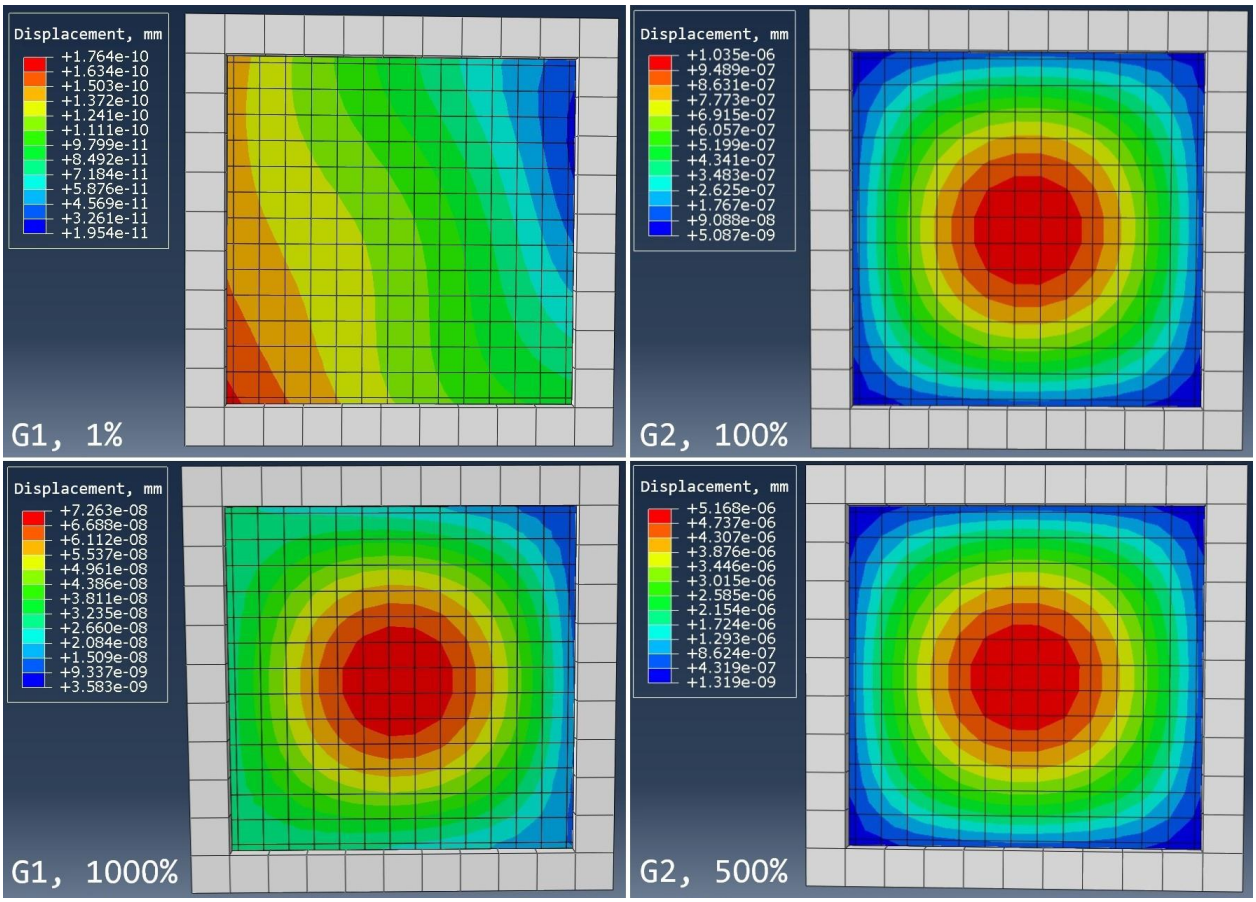

Figure 3.4. Displacement contours plotted onto the G1 and G2 gratings during loading. The upper left, upper right, and lower left gratings failed to show passing symmetry. The lower right grating shows passing symmetry.

measuring central node displacement after applying a clinically-relevant load. We have defined the relationship with a least squares regression line as shown in Figure 3.6. Pearson's r values for the correlation between inverse Young's modulus and central element displacement for the G0, G1, and G2 gratings are respectively 0.999361, 0.999000, and 0.999898. These high correlation values exceed the validation criterion and demonstrate good elastic behavior of our grating volumes.

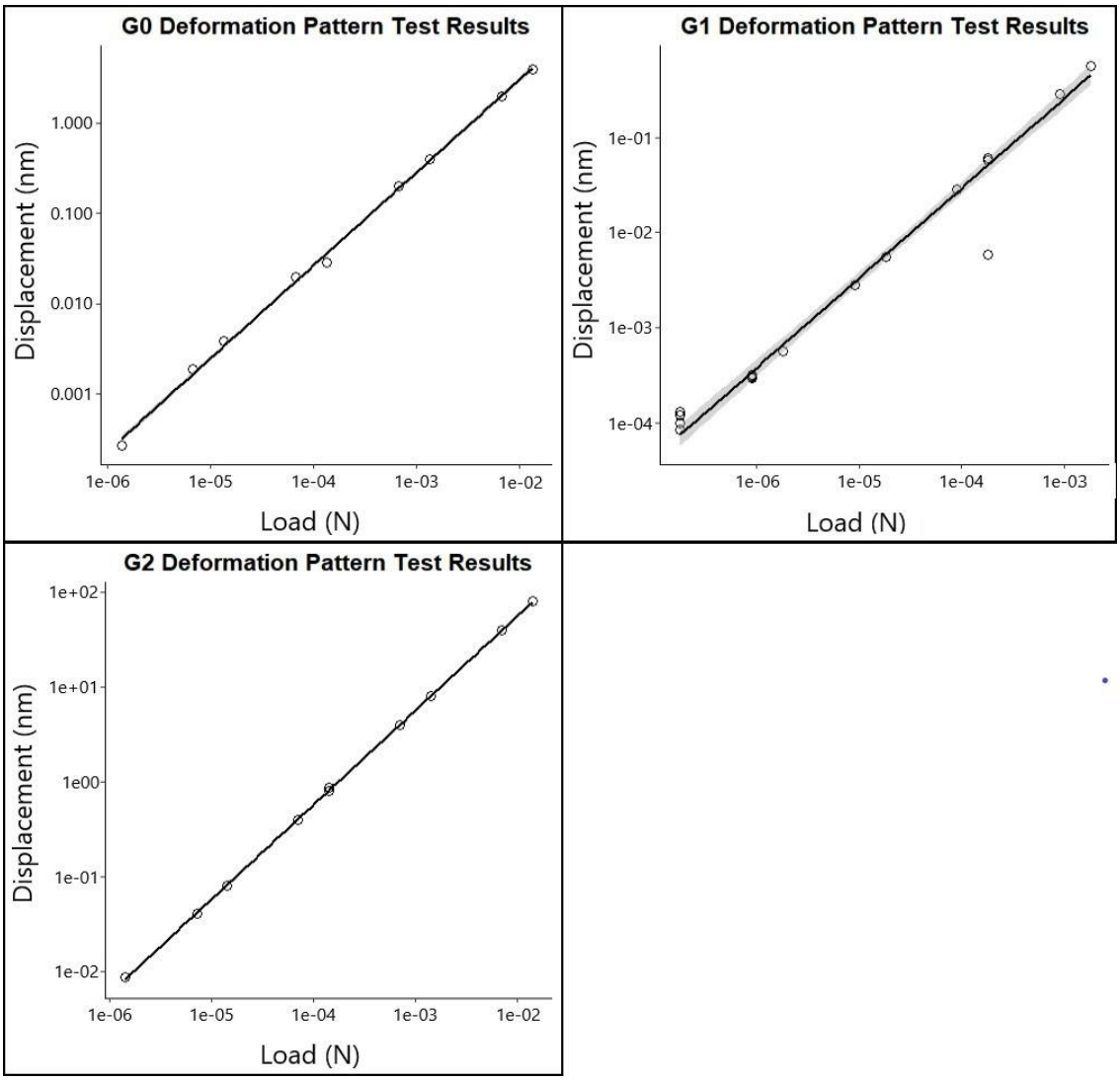

Figure 3.5. Plots of applied load vs. off-axis node displacement for all three gratings. Least squares regression lines have been fit to the data with respective Pearson's r coefficients of 0.999996, 0.998973, and 1.00000 for the G0, G1, and G2 gratings. The shaded area represents statistical uncertainty of the fit curve.

3.6. Load Distribution Test

We tested the validity of our approximation of the rotational load on the gratings in the FEA application as a uniform body force by comparing central and off-axis node displacement under uniform and nonuniform loading conditions at various distances from the center of rotation. The nonuniform load distribution takes into consideration the

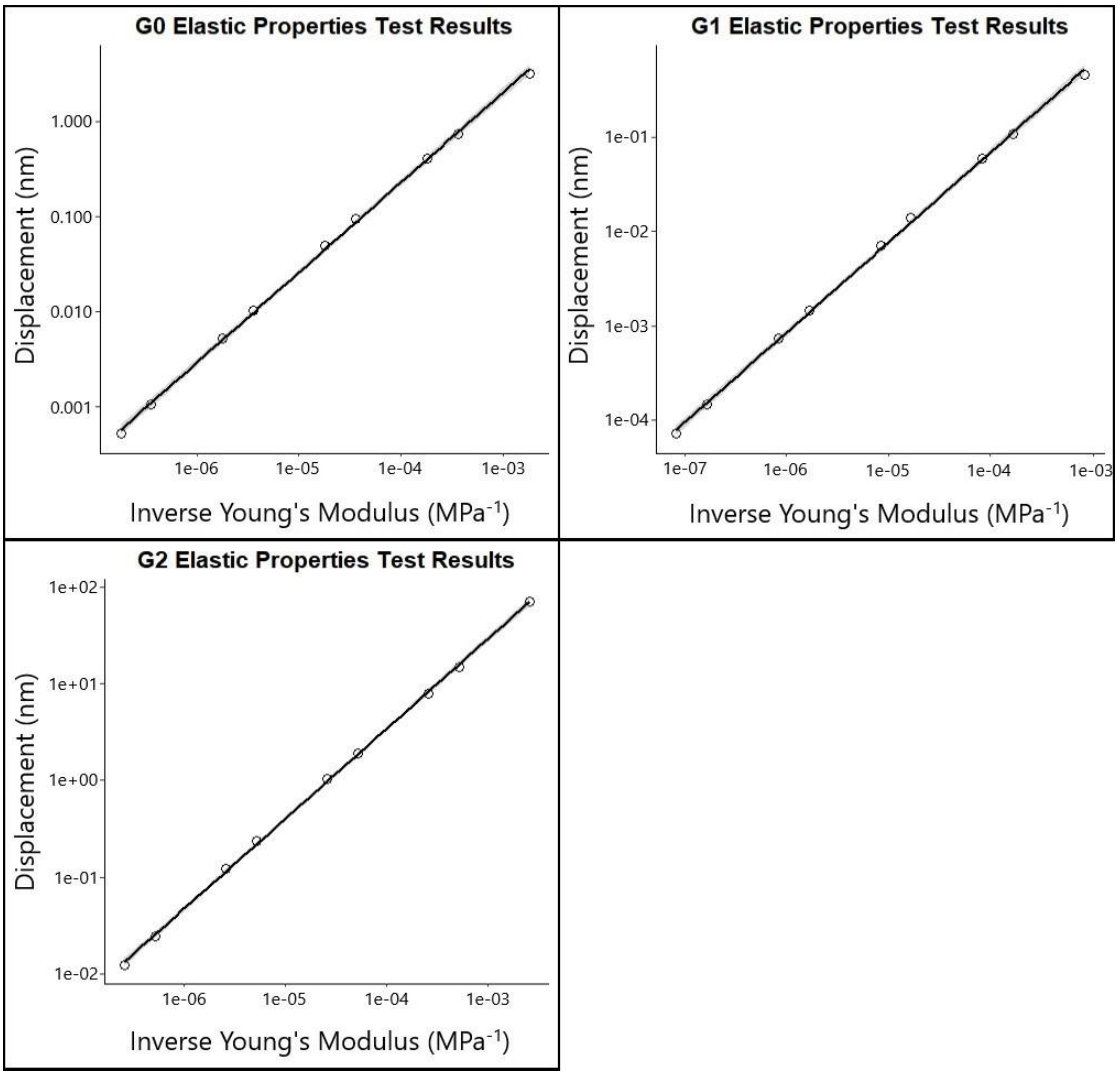

Figure 3.6. Plots of inverse Young's modulus vs. central element displacement for all three gratings. The shaded area represents statistical uncertainty of the fit curve.

increased force applied to the grating at the edges due to the greater distance from the center of rotation. Results are shown in Figure 3.7. The clear separation between displacement values resulting from the uniform and nonuniform loads indicates that the uniform load distribution is not a good approximation. There was more than an order of magnitude difference between uniform and nonuniform displacement values at all distances for both central and off-axis nodes. The displacement pattern was also different between

the two load distributions, which is demonstrated in Figure 3.8. Data was not collected for the G1 grating at 60, 70, 80, and 140% clinical distance because deformation from the nonuniform load was not significant enough to create good contact between the grating edges and the frame, causing Abaqus to abort the simulation.

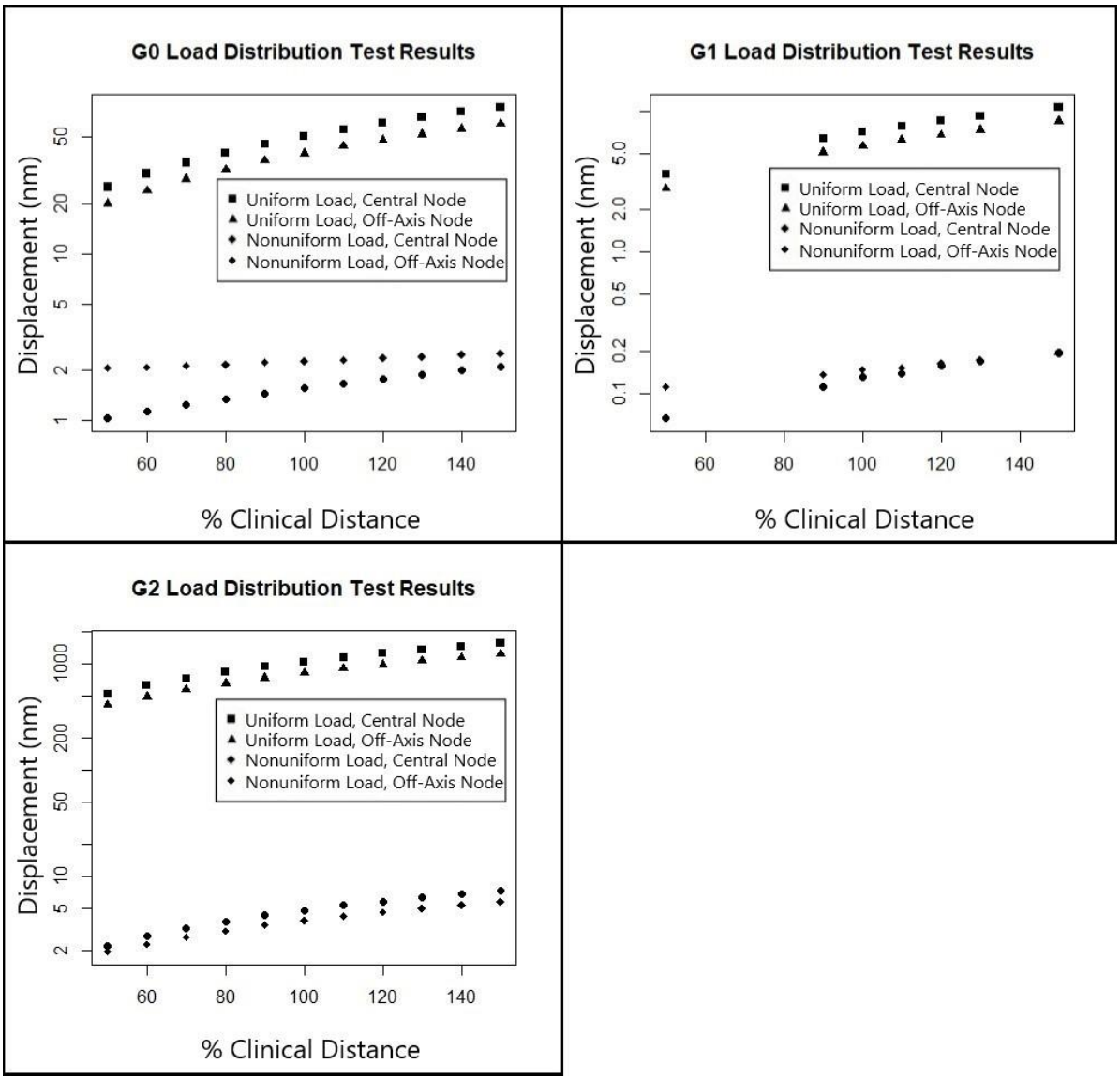

Figure 3.7. Plots of average node displacement vs. grating distance from the center of rotation for all three gratings placed under the uniform and nonuniform loads. Error bars are too small to visualize.

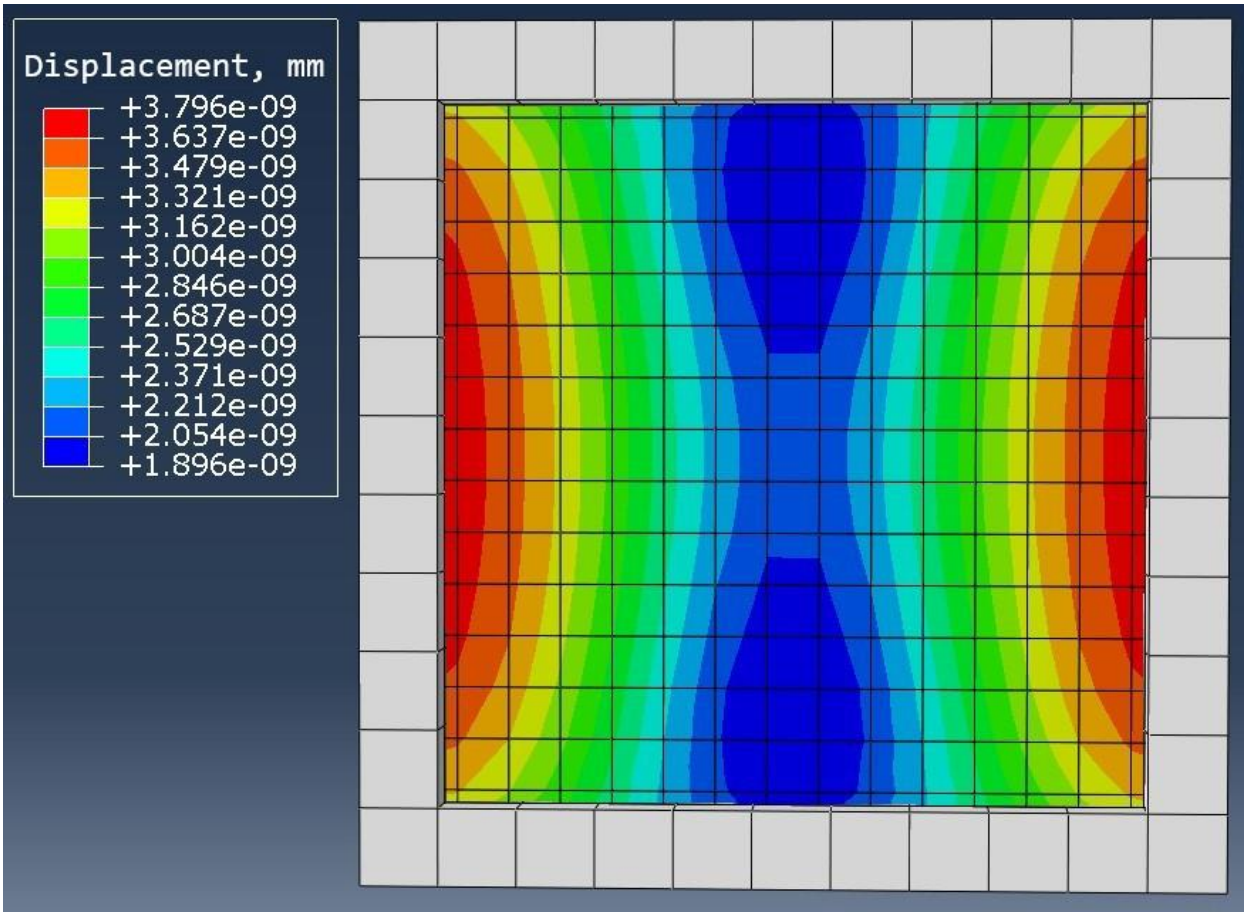

Figure 3.8. Displacement contours plotted onto the G0 grating under the nonuniform load at 150% clinical distance (88.5 cm). The displacement pattern is substantially different from that resulting from the uniform load such as in Figure 3.4.

Chapter 4. Discussion

We have created dosimetry applications for radiography and CT TLXI devices using the TOPAS particle transport environment, as well as an FEA application for CT optical components using Abaqus. We have tested the basic properties of these applications to validate our geometry setup and demonstrate data collection methods. Testing has concluded that our radiography and CT applications correctly model attenuation and dosimetry of the photon beam in both the grating and patient materials. We have further demonstrated a method to prepare input CT data and collect tissue-specific dose metrics using image processing techniques. We have shown that our FEA application maintains good contact between interacting volumes for loads above 10^{-7} N if a contact step is added to the data collection protocol described in Section 2.2.3. We have shown that the elastic behavior of the grating volumes varies appropriately with both the applied load and the Young's Modulus of the grating material. We have ruled out a uniform approximation of the load distribution across the grating volume in favor of a model which applies more realistic rotational mechanics. Our applications have proven to be robust and ready for evaluation of prototype geometries for TLXI devices.

The work we have presented here can be interpreted as preliminary results demonstrating the viability of TLXI lung imaging systems. Attenuation testing was performed with parameter values (e.g., component positions and thicknesses, acquisition parameters) which we anticipate will be used in prototype designs. These results show that our radiography and CT designs deliver equal-quality diagnostic data with acceptable increase to patient dose. Comparing the gratings-enabled and gratings-disabled dosimetry data from our attenuation tests, we can conclude that our TLXI radiography and CT

systems respectively deliver a factor of about 3.53 and 3.63 greater patient dose than the traditional setup. These results approach the expectations set by Willer *et al.* (2018), who calculated a patient dose increase of 260% from *in vivo* measurements using their prototype TLXI lung radiography scanner. Our approximation of the gratings as homogeneous slabs with no patterning features causes our results to overestimate beam attenuation and the corresponding dosimetry by about 30%. Additionally, Vedantham *et al.* (2014) have shown in Monte Carlo simulations of a TLXI mammography system that the G2 grating can act as a scatter grid, reducing the contribution of incoherent scatter to detector signal by as much as 35%. The decreased scatter-to-primary signal ratio allows comparable quality images to be acquired with lower patient dose. Using our results as the worst case scenario, a patient scanned with our TLXI radiography device can expect to receive as much as 0.253 mSv more dose than with the traditional setup and an associated increased risk of radiation-induced mortality of 0.001265%, while a patient scanned with our TLXI CT device can expect to receive up to an additional 18.41 mSv and an increased risk of mortality of 0.09205% (Protection, 2007).

Additionally, FEA results show that our CT design can operate with clinically relevant pitch and scan time without significantly deforming optical components under rotational load. Testing was performed with grating thicknesses which are at least an order of magnitude thinner than the clinical design, which makes our results more cautious than necessary since thinner gratings should be more flexible. Thus, the load distribution tests may be taken as a preliminary indication that the grating deformation from CT gantry rotation to be on the order of tens of nanometers at the most. We expect negligible disturbance of the Talbot carpet since the trench width of each grating is on the

order of a few microns. Of more concern is the shift in grating alignment due to the changing direction of the gravity vector relative to the plane of the grating during gantry rotation, which has been shown to cause phase variations as great as 12π in prototype phase contrast CT systems (Tapfer *et al.*, 2012). Overall, our results suggest that a TLXI prototype using our grating specifications will be able to acquire quality diagnostic data with acceptable increase in patient dose and negligible disruption due to grating deformation.

There are several ways in which this study could be improved. Testing for the radiography and CT applications would have yielded more robust single-material attenuation data with higher-statistics runs. We could have measured the transmission through the bone phantom blocks by increasing the number of histories above 200,000,000. Fortunately, it is not strictly necessary to validate TOPAS material attenuation properties since its basic functions have been thoroughly validated (Perl *et al.*, 2012). As well, the history counts used in attenuation tests for were well below the number of photons used in a clinical scan. Working backwards from the expected patient dose from a chest radiography scan, we see that approximately

$$\frac{1.0*10^{-4}\frac{Gy}{scan}*1\frac{\frac{J}{kg}}{Gy}*1\frac{g}{cm^3}(41.6\ cm*27.8\ cm*52.4\ cm)}{1.602*10^{-16}\frac{J}{keV}*70.7\frac{keV}{photon}*1000\frac{g}{kg}} \cong 5.4*10^{11}\frac{photons}{scan} \qquad (4.1)$$

are required to achieve acceptable image quality. Thus, our simulation history count would have to be increased by more than 4 orders of magnitude to simulate a clinical scan. We expect dosimetry results to scale proportionally with the history count, but our results

would be more clinically comparable if testing could be done with higher statistics on a high-performance computing system.

The CT scan used for the phantom volume was limited in many ways. First, the RANDO phantom itself is not perfectly anatomical. There were no delineations for organs other than the lungs and the helical overlap artifact caused large regions within a few slices to register as the incorrect tissue in TOPAS's material conversion process. The scan was adequate for comparing different simulation setups, but dosimetry data would be more directly comparable to clinical scenarios if the heart, esophagus, and spinal cord could be clearly identified. Steps were taken to make the phantom more anatomical, such as downsampling and digital removal of holes, but these were too time-consuming to facilitate rapid testing. Ideally, testing would be performed using an anonymized patient CT scan. Second, the phantom was not paired with an RTDose module which could have contoured organs for dose assessment. The thresholding method we have used to define tissue types carries undue uncertainty since many voxels which should not be of the same tissue type share the same HU values, especially in regions with the helical artifact. For example, the small gradient between high- and low-density regions such as the air-skin interface registered as lung, as is apparent in Figure 2.7.

Broad beam geometry made it difficult to confirm proper attenuation of grating and patient materials. Test results would be more accurate if downstream scoring volume was constrained to the original width of the beam and positioned further away from the material slab. This would exclude secondary particles and from simulation measurements and allow us to include coherently scattered photons in hand calculations. In the keV range, coherent scatter has a significant effect on the beam, which is material-dependent.

The attenuation coefficient of gold, for instance, is increased by 14% when coherent scatter is included.

Approximating the gratings as homogeneous slabs imparts systematic uncertainty to our application results which may make them less useful for predicting real-world scenarios. For the dosimetry applications, differences in the energy fluence spectrum of the transmitted beam could be accounted for by breaking the simulation into discrete stages, where each stage constitutes the particle transport occurring between a given pair of gratings. The beam spectrum would be redefined at the downstream surface of each grating, with half of its energy fluence retaining the spectral characteristics of the beam just prior to interaction with the grating. The second half of the energy fluence would be modified as if it had passed through the full thickness of attenuating material and then superimposed to include both the effects of the bars and trenches in the grating pattern. The resulting energy fluence spectrum would be more heavily weighted toward the lower energies since low-energy photons are not uniformly filtered out of the beam.

For the FEA applications, differences in the pattern and magnitude of deformation under load could be assessed by modeling small, isolated pieces of the grating. Each piece would consist of parallel metal bars fixed at each end and spaced according to the pitch of the grating pattern. Higher Young's modulus would cause the gratings to deform about 33% less. However, fewer stabilizing connections in the direction perpendicular to the grating lines would result in greater deformation, especially toward the edges of the grating.

Chapter 5. Conclusion

This study is part of a larger effort to put TLXI diagnostic medical imaging devices into clinical use. The software toolkit we have described is intended to be utilized by multiple users who are not necessarily specialists in the software or in medical physics. The radiography and CT applications have been designed so that only basic knowledge of the TOPAS environment is required for use. Multiple configurations have been created for both setups to suit varying requirements for device footprint. Accessory scripts for image processing and parameter generation require minimal user input and are commented throughout with labeling and instructions. Video tutorials have been recorded which demonstrate manipulation and execution of TOPAS and Abaqus simulations. We expect future users to employ the methods described in Section 2.2.1 to compile a catalog of dose and acquisition parameters (e.g., grating dimensions, grating placement, filtration thickness, effective beam energy, history count, pitch) for the radiography and CT setups. This will allow selection of the most optimized geometry and acquisition protocol for device prototyping.

Future users may wish to further the development of the software toolkit by expanding its testing capabilities. Thermal and gravitational dynamics could be incorporated into the FEA application to more holistically assess the factors influencing grating structure. Grating volumes could be modified to represent the edge-on design described by Thüring *et al.* (2014) to improve structural integrity. radiography and CT application testing could be repeated using an anonymized patient CT scan paired with RTDose contouring to assess organ-specific dosimetry and other imaging sites such as the pelvis and lower limbs.

We created and tested software applications for dosimetry and finite element analysis of chest imaging platforms which use a Talbot-Lau x-ray interferometry design. Testing has shown that our applications simulate the imaging environment with sufficient realism to assess the performance of candidate device geometries. Future users will use these tools to select the prototype design for clinical diagnostic conventional radiography and computed tomography devices.

References

Agostinelli, Sea *et al.* (2003). "GEANT4—a simulation toolkit". In: *Nuclear Instruments and Methods in Physics Research Section A: Accelerators, Spectrometers, Detectors and Associated Equipment* 506.3, pp. 250–303.

Attix, Frank Herbert (2008). *Introduction to Radiological Physics and Radiation Dosimetry*. John Wiley and Sons.

Bech, Martin *et al.* (2013). "In-vivo dark-field and phase-contrast x-ray imaging". In: *Scientific Reports* 3.1, pp. 1–3.

Berger, Martin *et al.* (1999). *XCOM: Photon Cross Section Database (version 1.2)*.

Borgesson, L (1996). "Abaqus". In: *Developments in Geotechnical Engineering*. Vol. 79. Elsevier, pp. 565–570.

Bushberg, Jerrold T and John M Boone (2011). *The Essential Physics of Medical Imaging*. Lippincott Williams and Wilkins.

Cao, Yanan *et al.* (2020). "Image artifacts caused by incorrect bowtie filters in cone-beam CT image-guided radiotherapy". In: *Journal of Applied Clinical Medical Physics* 21.7, pp. 153–159.

Carver, DE *et al.* (2015). "Development and validation of a GEANT4 radiation transport code for CT dosimetry". In: *Health Physics* 108.4, p. 419.

Collaboration, GEANT *et al.* (2016). "Physics reference manual". In: *URL https://geant4-userdoc.web.cern.ch/UsersGuides/PhysicsReferenceManual/BackupVersions/V10.6c/fo/PhysicsReferenceManual.pdf* 9.0.

Collaboration, Geant *et al.* (2019). "Book For Application Developers". In: *URL https://geant4-userdoc.web.cern.ch/UsersGuides/ForApplicationDeveloper/BackupVersions/V10.6c/fo/BookForApplicationDevelopers.pdf* 10, pp. 5–2.

Faddegon, Bruce *et al.* (2020). "The TOPAS tool for particle simulation, a Monte Carlo simulation tool for physics, biology and clinical research". In: *Physica Medica* 72, pp. 114–121.

Fritsch, Andreas, Luc Dormieux, and Christian Hellmich (2006). "Porous polycrystals built up by uniformly and axisymmetrically oriented needles: homogenization of elastic properties". In: *Comptes Rendus Mécanique* 334.3, pp. 151–157.

Gierada, David S *et al.* (2007). "Comparison of standard-and low-radiation-dose CT for quantification of emphysema". In: *American Journal of Roentgenology* 188.1, pp. 42–47.

Hellbach, Katharina *et al*. (2015). “In vivo dark-field radiography for early diagnosis and staging of pulmonary emphysema”. In: *Investigative Radiology* 50.7, pp. 430–435.

Henschke, Claudia I *et al*. (1999). “Early Lung Cancer Action Project: overall design and findings from baseline screening”. In: *The Lancet* 354.9173, pp. 99–105.

Hopcroft, Matthew A, William D Nix, and Thomas W Kenny (2010). “What is the Young’s Modulus of Silicon?” In: *Journal of Microelectromechanical Systems* 19.2, pp. 229–238.

Humphrey, Linda L *et al*. (2013). “Screening for lung cancer with low-dose computed tomography: a systematic review to update the US Preventive services task force recommendation”. In: *Annals of Internal Medicine* 159.6, pp. 411–420.

Jacobs, Troy D (2020). “Visualization of Brown Fat Using X-ray Dark Field Imaging”. In: *Louisiana State University and Agricultural and Mechanical College Digital Commons*.

Lynch, David A (2014). “Progress in imaging COPD, 2004-2014”. In: *Chronic Obstructive Pulmonary Diseases: Journal of the COPD Foundation* 1.1, p. 73.

Meinel, Felix G *et al*. (2014). “Improved diagnosis of pulmonary emphysema using in vivo dark-field radiography”. In: *Investigative Radiology* 49.10, pp. 653–658.

Michel, Thilo *et al*. (2013). “On a dark-field signal generated by micrometer-sized calcifications in phase-contrast mammography”. In: *Physics in Medicine and Biology* 58.8, p. 2713.

Miled, K, Karam Sab, and Robert Le Roy (2011). “Effective elastic properties of porous materials: Homogenization schemes vs experimental data”. In: *Mechanics Research Communications* 38.2, pp. 131–135.

Morgan, Elise F., George L. Barnes, and Thomas A. Einhorn (2013). “Chapter 1 - The Bone Organ System: Form and Function”. In: *Osteoporosis (Fourth Edition)*. Ed. by Robert Marcus *et al*. Fourth Edition. San Diego: Academic Press, pp. 3–20.

Neck, Daniel (2021). In: *Private Communication* May, 2021.

Patwa, Apeksh and Amit Shah (2015). “Anatomy and physiology of respiratory system relevant to anaesthesia”. In: *Indian Journal of Anaesthesia* 59.9, p. 533.

Perl, Joseph *et al*. (2012). “TOPAS: an innovative proton Monte Carlo platform for research and clinical applications”. In: *Medical Physics* 39.11, pp. 6818–6837.

Pfeiffer, F (2019). “Ten years from bench to bedside - Key achievements and pitfalls on the way to first patient results of grating-based darkfield chest X-ray radiography”. In: *X-ray and Neutron Phase Imaging with Gratings*.

Pfeiffer, F *et al*. (2009). “X-ray dark-field and phase-contrast imaging using a grating interferometer”. In: *Journal of Applied Physics* 105.10, p. 102006.

Pfeiffer, Franz *et al*. (2008). “Hard-X-ray dark-field imaging using a grating interferometer”. In: *Nature Materials* 7.2, pp. 134–137.

Poludniowski, Gavin *et al*. (2009). “SpekCalc: a program to calculate photon spectra from tungsten anode x-ray tubes”. In: *Physics in Medicine and Biology* 54.19, N433.

Poludniowski, Gavin G (2007). “Calculation of x-ray spectra emerging from an x-ray tube. Part II. X-ray production and filtration in x-ray targets”. In: *Medical Physics* 34.6Part1, pp. 2175–2186.

Poludniowski, Gavin G and Philip M Evans (2007). “Calculation of x-ray spectra emerging from an x-ray tube. Part I. Electron penetration characteristics in x-ray targets”. In: *Medical Physics* 34.6Part1, pp. 2164–2174.

Protection, Radiological (2007). “ICRP publication 103”. In: *Annals of the ICRP* 37.2.4, p. 2.

Scherer, Kai, Eva Braig, *et al*. (2016). “Improved diagnostics by assessing the micromorphology of breast calcifications via x-ray dark-field radiography”. In: *Scientific Reports* 6.1, pp. 1–11.

Scherer, Kai, Andre Yaroshenko, *et al*. (2017). “X-ray dark-field radiography-in-vivo diagnosis of lung cancer in mice”. In: *Scientific Reports* 7.1, pp. 1–9.

Schneider, Wilfried, Thomas Bortfeld, and Wolfgang Schlegel (2000). “Correlation between CT numbers and tissue parameters needed for Monte Carlo simulations of clinical dose distributions”. In: *Physics in Medicine and Biology* 45.2, p. 459.

Sidhaye, Venkataramana K, Kristine Nishida, and Fernando J Martinez (2018). “Precision medicine in COPD: where are we and where do we need to go?” In: *European Respiratory Review* 27.149.

Strobl, Markus (2014). “General solution for quantitative dark-field contrast imaging with grating interferometers”. In: *Scientific Reports* 4.1, pp. 1–6.

Tapfer, Arne *et al*. (2012). “Experimental results from a preclinical X-ray phase-contrast CT scanner”. In: *Proceedings of the National Academy of Sciences* 109.39, pp. 15691–15696.

Thüring, Thomas *et al*. (2014). “X-ray phase-contrast imaging at 100 keV on a conventional source”. In: *Scientific Reports* 4.1, pp. 1–4.

Thurston, Jim (2010). “NCRP Report No. 160: Ionizing Radiation Exposure of the Population of the United States”. In: *Physics in Medicine and Biology* 55.20, pp. 6327–6327.

Vedantham, Srinivasan, Linxi Shi, and Andrew Karellas (2014). “Large-angle x-ray scatter in Talbot–Lau interferometry for breast imaging”. In: *Physics in Medicine and Biology* 59.21, p. 6387.

Viermetz, Manuel *et al*. (2022). “Dark-field computed tomography reaches the human scale”. In: *Proceedings of the National Academy of Sciences* 119.8, e2118799119.

Vignero, J (2018). “Exploration of clinical applications of Talbot-Lau interferometry”. In: *Katholieke Universiteit Leuven*.

Willer, Konstantin, Alexander A Fingerle, Lukas B Gromann, *et al*. (2018). “X-ray dark-field imaging of the human lung—A feasibility study on a deceased body”. In: *PLoS One* 13.9, e0204565.

Willer, Konstantin, Alexander A Fingerle, Wolfgang Noichl, *et al*. (2021). “X-ray dark-field chest imaging for detection and quantification of emphysema in patients with chronic obstructive pulmonary disease: a diagnostic accuracy study”. In: *The Lancet Digital Health* 3.11, e733–e744.

Willner, M *et al*. (2014). “Quantitative breast tissue characterization using grating-based x-ray phase-contrast imaging”. In: *Physics in Medicine and Biology* 59.7, p. 1557.

Yang, Kai *et al*. (2019). “Data of CT bow tie filter profiles from three modern CT scanners”. In: *Data in Brief* 25, p. 104261.

Yaroshenko, Andre *et al*. (2015). “Improved in vivo assessment of pulmonary fibrosis in mice using x-ray dark-field radiography”. In: *Scientific Reports* 5.1, pp. 1–8.

Zienkiewicz, Olek C, Robert L Taylor, and Jian Z Zhu (2005). *The Finite Element Method: Its Basis and Fundamentals*. Elsevier.

Vita

Charles Zimmerman was born in Massachusetts in 1996. Charles grew up in Salt Lake City, Utah and attended Jordan High School. He graduated from Jordan in 2014. In 2014 he enrolled at the University of Utah, where he received his Bachelor of Science degree in Physics. After graduating from the University of Utah in the spring of 2019, he matriculated into the Medical Physics Master of Science Program at Louisiana State University. Following graduation from the medical physics program in August of 2022, he will begin residency at the Ohio State University.